CrossMark

REVIEW ARTICLE

Role of liquid repellency on fluid slip, fluid drag, and formation of nanobubbles

Bharat Bhushan[1]

Abstract The reduction of fluid drag is of scientific interest in many fluid flow applications. Fluid flow is known to have zero slip on liquiphilic surfaces, and the relative velocity between a solid wall and liquid flow is zero at the solid–liquid interface. However, boundary slip is known to occur on liquiphobic (both hydrophobic and oleophobic) surfaces. In this paper, we present an overview of data on fluid slip on liquiphilic/phobic surfaces and generation of nanobubbles on hydrophobic surfaces. The fluid slip facilitates fluid flow and is believed to result in lower fluid drag, of interest in many applications. Generation of nanobubbles can also be used for various biomedical applications.

1 Introduction

The reduction of fluid drag is of scientific interest in many fluid flow applications, including micro/nanofluidic systems used in biological, chemical, and medical fields (Bhushan 2016, 2017a, b). Fluid flow is known to have zero slip on liquiphilic surfaces. In the no-slip boundary condition, the relative velocity between a solid wall and liquid flow is zero at the solid–liquid interface (Batchelor 1970). However, boundary slip implies of a relative motion between solid and liquid adjacent to the solid surface, and is known to occur on liquiphobic (both hydrophobic and oleophobic) surfaces (Wang et al. 2009a; Jing and Bhushan 2013a; Li and Bhushan 2015). The degree of slip can be characterized by the so-called slip length that is the vertical distance below the solid at which the velocity of the fluid flow extrapolates to zero, as shown schematically in Fig. 1. It is generally measured using atomic force microscopy (AFM) both in the contact mode and tapping mode (Wang and Bhushan 2010; Maali and Bhushan 2012; Maali et al. 2016). The slip length for liquiphobic surfaces has been reported to be in the range of few nm to several μm. The boundary slip condition represents lower hydrodynamic fluid drag as compared to that of a surface with zero slip (Watanabe et al. 1999; Ou et al. 2004; Shirtcliffe et al. 2009; Maali and Bhushan 2013; Jing and Bhushan 2013c, 2015; Li et al. 2016).

Air bubbles on the nanoscale, referred to as "nanobubbles" are found to be present on the smooth liquiphobic surfaces. Their size ranges from few nm to several microns. They have been observed by imaging with an atomic force microscope in the tapping mode (Wang and Bhushan 2010; Mazumder and Bhushan 2011; Maali and Bhushan 2013; Li et al. 2016). Nanobubbles are believed to be one of factors responsible for boundary slip (Wang et al. 2009a; Maali and Bhushan 2013; Li et al. 2016.). The degree of liquiphobicity, surface roughness, surface charge, electric field, and pH of the fluid, and gas concentration in the fluid are some of the parameters which affect propensity of nanobubbles, boundary slip, and fluid drag (Wang et al. 2009a; Jing and Bhushan 2013a; Mazumder and Bhushan 2011; Pan et al. 2014; Jing and Bhushan 2015; Li and Bhushan 2015; Li et al. 2016).

In this paper, we first describe AFM based measurement technique to measure fluid slip and to image nanobubbles, followed by representative data on fluid slip on liquiphilic/phobic surfaces and generation of nanobubbles on hydrophobic surfaces.

✉ Bharat Bhushan
bhushan.2@osu.edu

[1] Nanoprobe Laboratory for Bio- and Nanotechnology and Biomimetics, Ohio State University, 201 W. 19th Ave, W390 Scott Laboratory, Columbus, OH 43210, USA
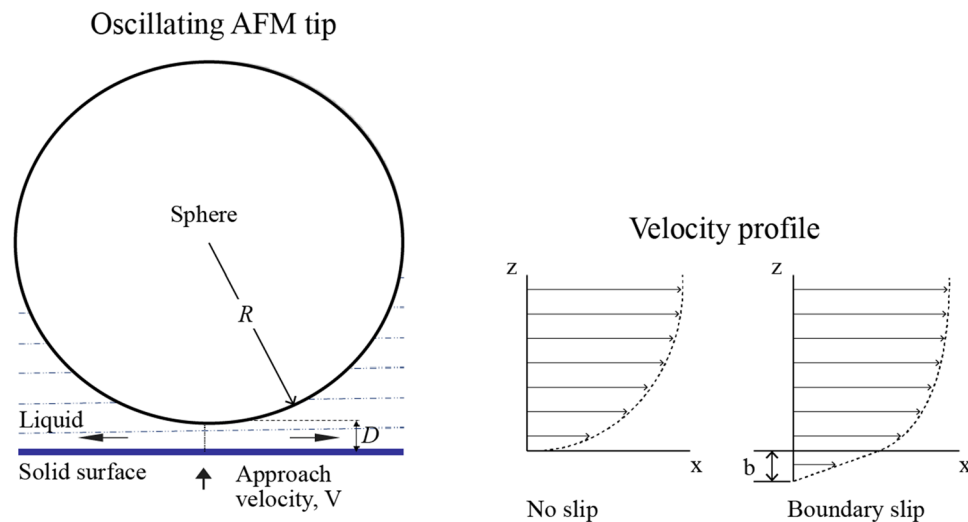
Fig. 1 Schematics of an oscillating spherical AFM tip approaching a surface with a velocity (*left*) and velocity profiles of fluid flow with and without boundary slip (*right*) in the AFM method. The slip length

b provides a measure of boundary slip at the solid–liquid interface. During the approach process, the cantilever deflection as a function of separation distance data is recorded to calculate the slip length

2 Measurement techniques for boundary slip and nanobubbles

2.1 Measurement of boundary slip

A number of measurement techniques have been used to measure boundary slip. Some of the most commonly used techniques include capillary method, fluid flow tracing method, and liquid drainage method (Wang and Bhushan 2010; Maali and Bhushan 2012; Maali et al. 2016). In the capillary method, pressure drop of liquid flowing in a thin capillary pipe or channel between its two ends and the flow rate are measured. The boundary slip will increase the flow rate for a given pressure drop. For Navier slip boundary condition, the relationship between the slip length, volume flow rate, and pressure drop is used to calculate slip length. The capillary method is easy to use, however, issues relative to different flow conditions close to inlets and outlets and the middle of the pipe and lack of uniform geometry throughout the pipe are some of the concerns.

In the fluid flow tracing method, the fluid flow is directly observed by using either optical traceable particles or fluorescent molecules as velocity probes. In a commonly used particle image velocimetry (PIV) method, optically traceable small particles in the fluid flow are monitored for some period and velocity field of the local fluid is determined. The velocity field is used to calculate the slip length. The size of the particles is restricted by the laser wavelength, therefore the resolution is poor.

The most popular method used to measure boundary slip is the liquid drainage method using surface force

apparatus (SFA) or AFM. In this method, hydrodynamic drainage force (Fh) between two crossed cylindrical surfaces (SFA) or a sphere and a planar surface (AFM) is measured as a function of the separation distance (D) when surfaces approach each other, as shown in Fig. 1 for a sphere of radius R approaching a planar surface at an approach velocity of V. In the SFA method, contact regions are on the order of tens of μm^2 and loads used are on the order of 10 mN or larger. In the AFM method, contact region is on the order of tens of nm^2 and is used at loads on the order of few nN. To study boundary slip on the nanoscale, AFM method is desirable. It can be used either in the so called contact mode or tapping mode and is widely used (Bhushan 2017a, b).

Analysis to calculate the slip length from measured hydrodynamic force as a function of separation distance is presented next followed by the description of AFM measurement technique.

2.1.1 Analysis to calculate the slip length based on liquid drainage method

For a case of no-slip boundary condition, the hydrodynamic force acting on a cylindrical or spherical surface placed on a flat surface is given as (Batchelor 1970),

$$F_h = \frac{6\pi \eta R^2}{D} V \tag{1}$$

where η is the dynamic viscosity of the liquid, D is the separation distance between two surfaces, R is the radius of the sphere or the cylinder, and $V = dD/dt$ (t is time) is the velocity of two surfaces approaching each other.

In the presence of partial slip at solid–liquid interface, Vinogradova (1995) derived a relationship for hydrodynamic force by solving the continuity equation and the Navier–Stokes equation of the fluid flow in the gap and using Navier boundary condition which states that the tangential velocity of fluid is proportional to the ratio of the velocity to the velocity gradient in a direction perpendicular to the solid walls,

$$v_{w,b} = \left. \frac{\partial v_w}{\partial z} \right|_{z=0} \qquad (2)$$

where v_w and $v_{w,b}$ are liquid velocity in liquid and at the solid–liquid interface, respectively, and b has the unit of length and is referred as slip length. The hydrodynamic force for the case of slip boundary condition is given as,

$$F_h = f^* \frac{6\pi \eta R^2}{D} V \quad \text{for } D << R \qquad (3)$$

where f^* is the correction parameter to describe the drainage of liquid between two hydrophobic surfaces with slip and changes based on the boundary conditions.

If the no-slip boundary condition is valid on each one of the two approaching surfaces, $f^* = 1$. For an asymmetric case, when boundary slip occurs on only one surface with a slip length value b, while there is no boundary slip at the other surface, f^* is given as

$$f^* = \frac{1}{4} \left\{ 1 + \frac{3D}{2b} \left[\left(1 + \frac{D}{4b} \right) \ln \left(1 + \frac{4b}{D} \right) - 1 \right] \right\} \qquad (4)$$

By taking the asymptotic expansion of Eq. (4) in the limit of large separation, $D >> b$, the ratio of approach velocity and hydrodynamic force on the sphere can be simplify expressed as (Cottin-Bizonne et al. 2008).

$$\frac{V}{F_h} = \frac{1}{6\pi \eta R^2} (D + b) \quad \text{for } D >> b \qquad (5)$$

The position at which the linear extrapolation of the curve V/F_h intercepts the separation distance (D) axis gives the slip length, b.

2.1.2 AFM measurement technique

To carry out the slip length measurement by AFM based liquid drainage method in a liquid environment, a liquid cell is used to introduce liquid between the tip and the sample, as shown in Fig. 2a (Wang et al. 2009a; Wang and Bhushan 2010). In the liquid cell, a liquid meniscus is formed between the glass slide of the cell and the sample surface that can effectively avoid fouling of the tip due to the evaporation of liquid. Based on Eq. (5), the slip length is obtained from the hydrodynamic force applied on the AFM tip approaching the sample surface.
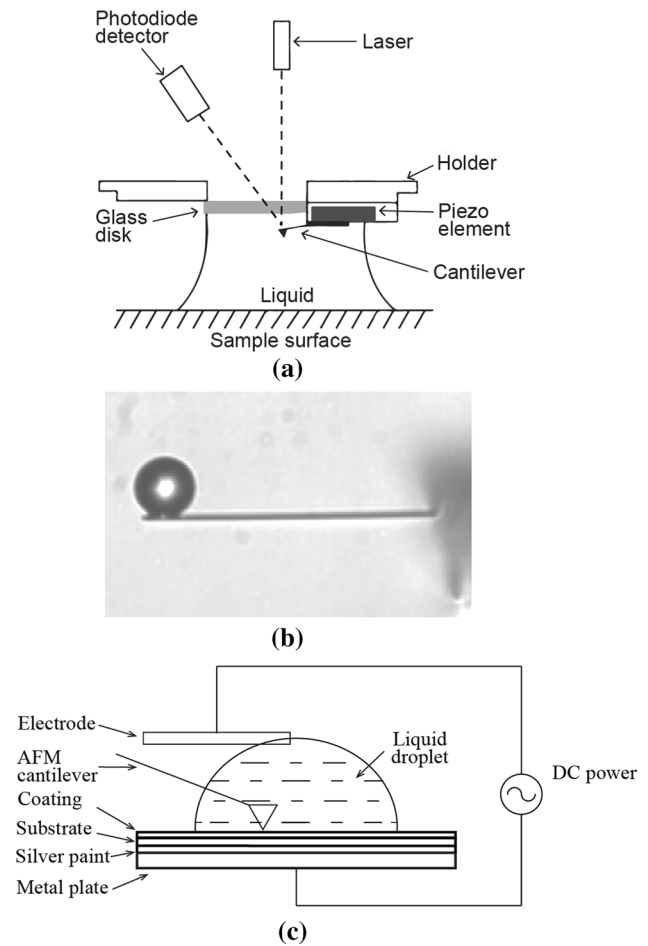
Fig. 2 a Schematic of an experimental setup used for slip length measurements and imaging of nanobubbles using a liquid cell in an AFM (Wang and Bhushan 2010), **b** optical image of the side view of AFM probe obtained by gluing a glass sphere at the end of a rectangular cantilever with a tip, and **c** schematic of the experimental setup used for the measurement of slip length as a function of applied voltage

Experimentally, the hydrodynamic force can be obtained by multiplying the AFM cantilever's deflection signal by the cantilever stiffness.

In order to perform AFM based liquid drainage experiments, an AFM colloidal probe is used, as shown Fig. 2b. The colloidal probe is prepared by gluing a borosilicate glass sphere (e.g., GL018B/45-33, Mo-Sci Corporation) or soda-lime silica sphere (9040 Duke Sci. Corp., Palo Alto, CA) with a diameter on the order of 30–60 μm on the AFM tip. A larger diameter of sphere on the order of 60 μm is used to increase the hydrodynamic force.

AFM can be used, either in the contact mode or tapping mode. The contact mode is more precise in force measurements but is generally used to measure small slip lengths found in liquids (Wang and Bhushan 2010; Li and Bhushan 2015). Tapping mode is often used for measurements of

large slip lengths such as in air (Maali and Bhushan 2008, 2012; Maali et al. 2016). For contact mode, a rectangular silicon cantilever-tip assembly of low stiffness of about 0.7N/m (e.g., ORC8, Bruker, resonance frequency of about 70 kHz) can be used and for the tapping mode, a rectangular silicon cantilever-tip assembly with high stiffness of 3 N/m (e.g., RFESP, Bruker, resonance frequency of about 73 kHz) can be used.

When the AFM colloidal probe approaches the sample with a constant velocity, the measured force includes hydrodynamic force and electrostatic force. Based on Eq. (3), the hydrodynamic force increases with the increasing approaching velocity. However, the electrostatic force remains constant. When the velocity is low enough, for example on the order of 0.22 μm s^{-1}, the hydrodynamic force is less than 0.1nN and can be neglected. Thus, the measured force can be considered as equal to the electrostatic force. When the velocity is large enough, for example on the order of 28 μm s^{-1}, the measured force includes both the hydrodynamic force and the electrostatic force. By subtracting the electrostatic force data obtained at low velocity from the measured force data obtained at high velocity, the hydrodynamic force used to obtain the slip length is effectively obtained. In addition, the separation distance between the spherical tip and the solid surface can be obtained by adding the sphere displacement and the cantilever deflection. V/F_h is plotted as a function of separation distance (D) and Eq. (5) is used to calculate the slip length.

To study the effect of electric field on the slip length, a nonconducting sample was glued to a metal plate which was used as an electrode with conductive silver paint (Pan and Bhushan 2013; Pan et al. 2014; Li and Bhushan 2015). A stainless wire was inserted into the droplet as another electrode. A DC power was applied to the two electrodes, as shown in Fig. 2c. In this experimental setup, the surface charge at the solid–liquid interface can be adjusted by changing the DC power.

2.2 Imaging of nanobubbles

A liquid cell used for boundary slip studies, is also used to study nanobubbles in the liquid environment (Wang and Bhushan 2010; Mazumder and Bhushan 2011; Maali and Bhushan 2013; Pan et al. 2014; Li et al. 2016). The AFM is used in tapping mode because the application of tapping mode can effectively reduce the force applied on the nanobubbles by the AFM tip and minimize its effect on the imaging of nanobubbles. A silicon cantilever-tip assembly (e.g., RFESP, Bruker with a stiffness resonance frequency of about 73 kHz) can be used.

3 Fluid slip measurements on liquiphilic/phobic surfaces

3.1 Hydrophilic/phobic surfaces

Liquid drainage experiments were carried out on hydrophilic/phobic samples using an AFM in contact mode, as well as in tapping mode as described earlier (Wang et al. 2009a; Bhushan et al. 2009). Wang et al. (2009a) used mica as the hydrophilic surface. Hydrophobic and superhydrophobic surfaces were prepared using molded epoxy as a substrate on which alkane n-hexatriacontane and Lotus wax (nonacosane-10, 15-diol and nonacosan-10-01), respectively, were deposited by thermal evaporation which self-assembled on the epoxy substrate. The roughness data (RMS and peak-to-mean distance) and contact angles are summarized in Table 1.

For the contact mode studies, cantilever deflection as a function of PZT vertical displacement data are presented in Fig. 3a. Next, the electrostatic force data obtained at low velocity was subtracted to obtain the hydrodynamic force component. The cantilever deflection was multiplied with the cantilever stiffness to obtain the hydrodynamic force data. The hydrodynamic force as a function of separation distance data for three samples is presented in Fig. 3b. The hydrodynamic force gradually increases with a decrease in the separation distance. The hydrodynamic force on the hydrophilic surface is the largest, followed by that on the hydrophobic and superhydrophobic surfaces.

The measured hydrodynamic force data is fitted in Eq. (5) to obtain the value of slip length. Slip length data are summarized in Table 1. Hydrophilic surfaces exhibit near zero slip. Hydrophobic and superhydrophobic surfaces exhibit slip with higher value for the latter. Wang et al. (2009a) reported that approach velocity in the range used had no effect on slip length. Additionally, the slip length

Table 1 RMS roughness and peak-to-mean distance (AFM scan size = 5 × 5 μm^2), contact angle, and slip length of three different surfaces

Surfaces	RMS roughness (nm)	Peak-to-mean distance (nm)	Contact angle (deg)	Slip length (nm)
Hydrophilic surface	0.2	0.4	∼0	∼0
Hydrophobic surface	11	34	91 ± 2.0	44 ± 10
Superhydrophobic surface	178	185	167 ± 0.7	257 ± 22

The variation represents ±1 standard deviation (Wang et al. 2009a)
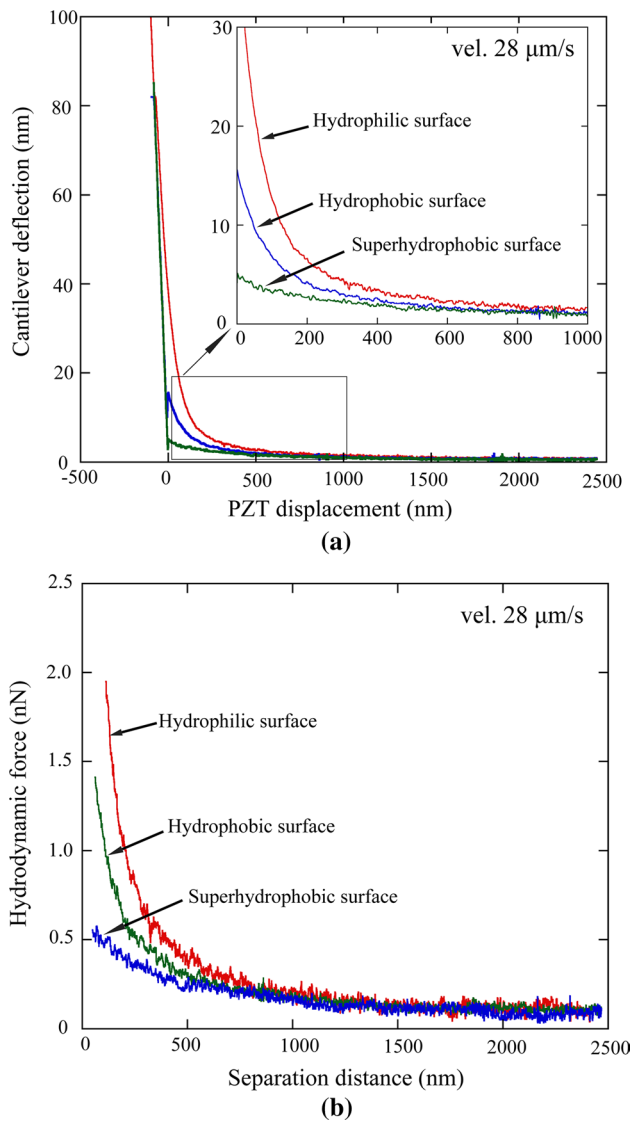
Fig. 3 **a** Measured cantilever deflection as a function of PZT displacement, and **b** calculated hydrodynamic forces a function of separation distance on the hydrophilic, hydrophobic, and superhydrophobic surfaces (various wax layers on epoxy) with an approach velocity of 28 μm/s (Wang et al. 2009a)

values were about the same in contact mode and tapping mode.

3.2 Oleophilic/phobic surfaces

Liquids with low surface tension, such as oils, are widely used in many fluid flow applications. The study of boundary slip on surfaces immersed in liquids with low surface tension is important, as well as its effect on fluid drag. Jing and Bhushan (2013a) measured fluid slip on oleophilic,

oleophobic, and superoleophobic surfaces which were all superhydrophobic. They compared the data with two hydrophobic samples—polystyrene (PS) and octadecyltrichlorosilane (OTS) self-assembled monolayer. Liquids used were DI water (71.99 mN/m), hexadecane (27.05 mN/m) and ethylene glycol (47.70 mN/m). To prepare superoleophilic and oleophobic surfaces, hydrophobic silica nanoparticles and methylphenyl silicone slurry was coated on the glass substrate with different particle-to-binder ratio (p–b ratio). To prepare superoleophobic surface, fluorinated acrylic copolymer coating was applied over nanoparticle-binder coating. The AFM images in air and roughness data for all five samples are presented in Fig. 4.
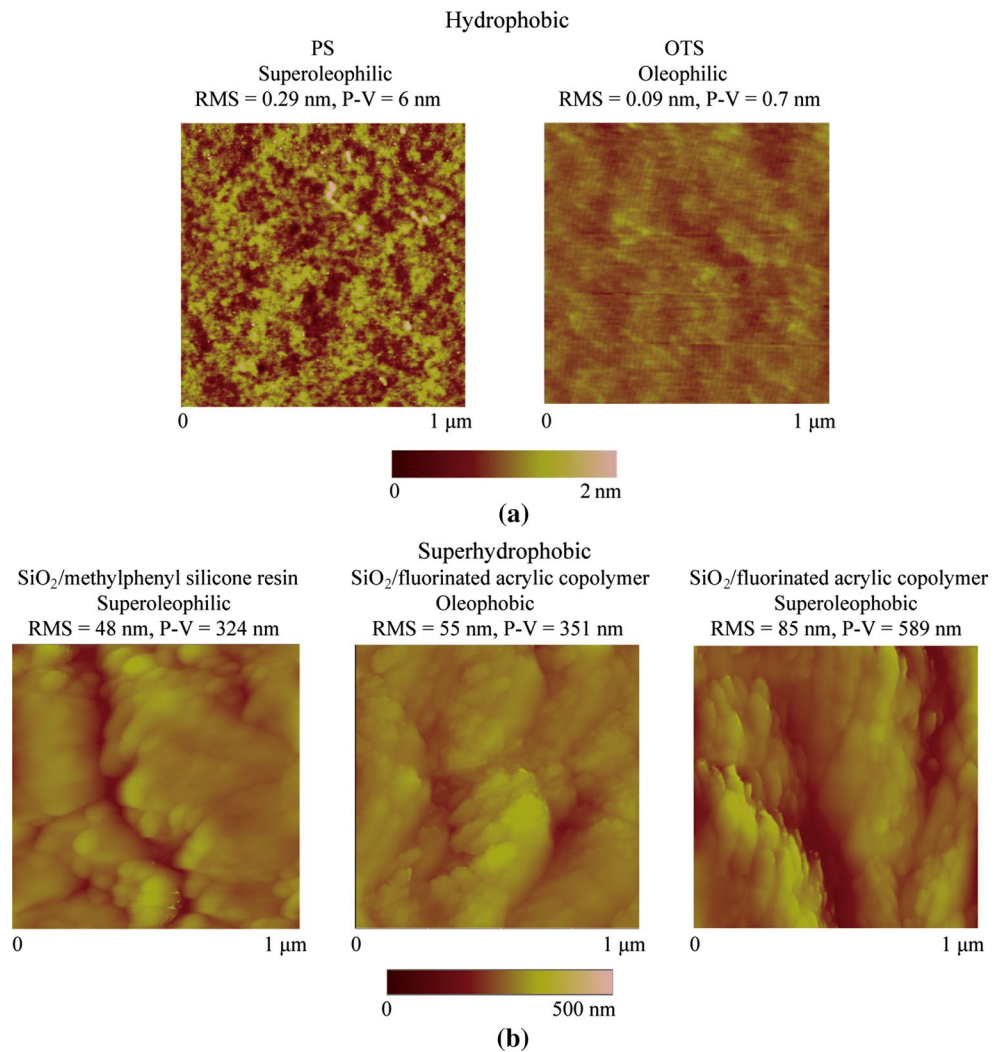
The coating thickness, contact angle, contact angle hysteresis and slip length of the five samples in contact with three liquids are presented in Table 2. The slip data are also summarized as a bar chart in Fig. 5 (Jing and Bhushan 2013a). From the results shown in Table 2 and Fig. 5, the slip length on the OTS surface is larger than that on the PS surface when immersed in the same liquid. The slip length of each sample immersed in deionized (DI) water is smallest, and the slip length of each sample immersed in ethylene glycol is largest. When samples with different degrees of oleophobicity are immersed in the same liquid, the slip length of the superoleophilic sample is smallest and the slip length on the superoleophobic sample is largest. The result can be explained by the fact that a larger contact angle leads to larger slip length. The possible mechanism is that a larger contact angle means that there will be a weaker interaction and smaller force between the solid surface and liquid molecules, which leads to larger slip length.

For both hydrophobic and superhydrophobic surfaces with different degrees of oleophobicity, the slip length of each sample immersed in DI water is the smallest, and the slip length of each sample immersed in ethylene glycol is the largest (Jing and Bhushan 2013a). The results are related to the viscosity of the liquid, presented in Table 3. By equating the viscous shear stress to the friction stress at the solid–liquid interface, Joly et al. (2006) expressed the slip length as following,

$$b = \eta/\mu \qquad (6)$$

where μ is the coefficient of friction between the liquid and the sample. According to Eq. (6), slip length is related to the viscosity of a liquid. For the same solid surface, a larger viscosity of liquid leads to a larger slip length. This can be used to explain the results of the slip length being the smallest for each sample when immersed in DI water and the slip length being the largest for each sample when immersed in ethylene glycol for both hydrophobic and superhydrophobic surfaces (Jing and Bhushan 2013a).

Fig. 4 AFM images in air and RMS roughness and *P–V* distance of **a** two hydrophobic–hydrophobic/superoleophilic and hydrophobic/oleophilic and **b** three superhydrophobic–superhydrophobic/superoleophilic, superhydrophobic/oleophobic, and superhydrophobic/superoleophobic surfaces (Li and Bhushan 2015)

Hydrophobic

PS
Superoleophilic
RMS = 0.29 nm, P-V = 6 nm

OTS
Oleophilic
RMS = 0.09 nm, P-V = 0.7 nm

0   1 µm   0   1 µm

0   2 nm

(a)

Superhydrophobic

SiO₂/methylphenyl silicone resin
Superoleophilic
RMS = 48 nm, P-V = 324 nm

SiO₂/fluorinated acrylic copolymer
Oleophobic
RMS = 55 nm, P-V = 351 nm

SiO₂/fluorinated acrylic copolymer
Superoleophobic
RMS = 85 nm, P-V = 589 nm

0   1 µm   0   1 µm   0   1 µm

0   500 nm

(b)

3.3 Effect of electric field and liquid pH on fluid slip

In aqueous solutions, most solid surfaces could be charged because of either the adsorption of ions or the dissociation of ionizable groups. The charge at the solid–liquid interface can strongly affect interfacial phenomena. The existence of surface charge at the solid–liquid interface has been found to affect the boundary slip (Joly et al. 2006; Jing and Bhushan 2013b, 2015; Pan and Bhushan 2013; Pan et al. 2014). Further, fluid flow is affected by the interfacial ion distribution and the so-called electrical double layer (EDL). This is caused by the surface charge at the solid–liquid interface based on electrostatic interaction (Jing and Bhushan 2013b, 2015). Various modeling and experimental studies have been performed to obtain the surface charge density at the interfaces (Jing and Bhushan 2015).

Applying an external electrical field to the solid–liquid interface and changing the pH of the liquid are two methods that can be used to control the surface charge. For a solid surface immersed in aqueous solution with applied electrical field, the surface polarizes in the applied electric field, as free electrons are redistributed to maintain equipotential. The absolute value of the surface charge is increased with applied negative electric field voltage (Pan and Bhushan 2013; Jing and Bhushan 2015; Li and Bhushan 2015).

The existence of surface charge is believed to affect the degree of slip. Joly et al. (2006) developed a theoretical model to study the effect of surface charge on the slip length based on molecular dynamics simulation. Experimental studies have also been carried out to analyze the effect of surface charge on slip length with an applied electric field or liquids with different pH values on hydrophobic surfaces immersed in saline solution and DI water (Jing and Bhushan 2013b; Pan and Bhushan 2013) and on superoleophilic, oleophilic, oloeophobic, and superoleophobic surfaces immersed in DI water and two oils with different surface tension (Li and Bhushan 2015).

Table 2 Coating thickness, contact angle (CA), contact angle hysteresis (CAH) and slip length of two hydrophobic and three superhydrophobic samples with three liquids (Jing and Bhushan 2013a)

Type of coating	Composition	Thickness (nm)	DI water			Hexadecane			Ethylene glycol		
			CA (°)	CAH (°)	Slip length (nm)	CA (°)	CAH (°)	Slip length (nm)	CA (°)	CAH (°)	Slip length (nm)
Hydrophobic											
Superoleophilic	Polystyrene (PS)	30 ± 10	94 ± 2	28 ± 3	~0	0	–	15 ± 4	54 ± 3	9 ± 3	40 ± 10
Oleophilic	Octadecyltrichlorosilane (OTS)	5 ± 3	106 ± 2	40 ± 4	30 ± 5	32 ± 2	18 ± 3	140 ± 50	84 ± 2	16 ± 3	200 ± 50
Superhydrophobic											
Superoleophilic	SiO$_2$ and methylphenyl silicone resin	700 ± 150	162 ± 5	7 ± 2	65 ± 20	8 ± 5	2 ± 1	80 ± 20	69 ± 3	9 ± 3	120 ± 20
Oleophobic	SiO$_2$, methylphenyl silicone resin and fluorinated acrylic copolymer (0.3% by weight)	700 ± 150	163 ± 3	12 ± 2	150 ± 30	100 ± 4	38 ± 6	350 ± 70	106 ± 4	24 ± 4	600 ± 100
Superoleophobic	SiO$_2$, methylphenyl silicone resin and fluorinated acrylic copolymer (0.6% by weight)	700 ± 150	165 ± 3	3 ± 1	300 ± 50	150 ± 5	11 ± 2	1350 ± 180	159 ± 6	7 ± 2	1800 ± 200
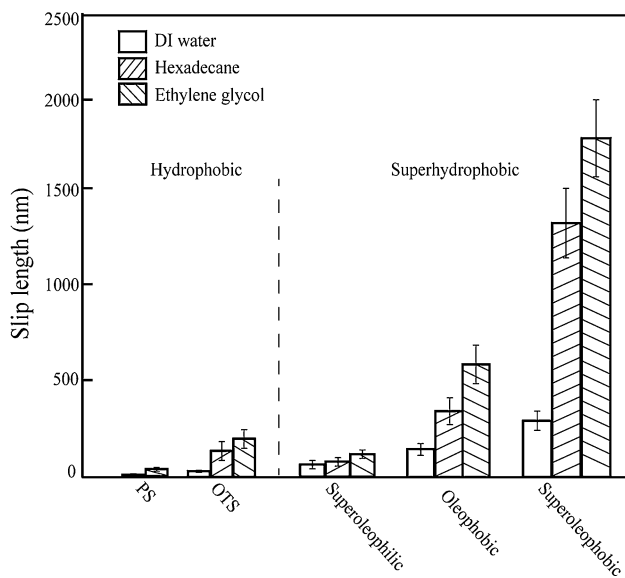
Fig. 5 Bar chart of slip length on the five samples immersed in DI water, hexadecane, and ethylene glycol (Jing and Bhushan 2013a)

**Table 3** Parameters of liquids used in the experiments (Haynes 2014)

Liquid	Surface tension (mN/m)	Dynamic viscosity (mPa s)
DI water	71.99	0.98
Hexadecane	27.05	3.03
Ethylene glycol	47.70	16.1

The slip lengths of hydrophobic OTS surface immersed in 0.01 and 0.15 M saline solutions and DI water as a function of applied voltage and pH values are shown in Fig. 6 (Jing and Bhushan 2013b). For the effect of the electric field, the slip length of OTS immersed in 0.15 M saline solution remains constant with an increasing positive voltage applied to the substrate. The slip length of OTS immersed in DI water remains constant with an increasing negative electric field value and increases with an increasing positive electric field value. For the effect of pH, the slip length of OTS immersed in 0.01 and 0.15 M saline solutions and DI water decreases with an increasing pH value. They correlated the effect of electric field and pH on slip to the calculated surface charge. Their results showed that a larger absolute value of the surface charge density led to a smaller slip length for different experimental conditions.

Figure 7a shows the slip length data as a function of applied voltage for two hydrophobic surfaces immersed in DI water, hexadecane and ethylene glycol (Li and Bhushan 2015). With a positive electric field applied to the substrate, the slip length of the PS surface in hexadecane and ethylene glycol increases with increasing applied voltage. However, the slip length of PS in DI water remains constant with increasing applied voltage. The slip lengths of OTS in DI water, hexadecane, and ethylene glycol increase with increasing applied voltage.

The effect of surface charge on the slip length can be given by using the physical model given by Joly et al. (2006),

$$b = \frac{b_0}{1 + (1/\alpha)(\sigma d^2/e)^2 (l_B/d^2) b_0} \tag{7}$$
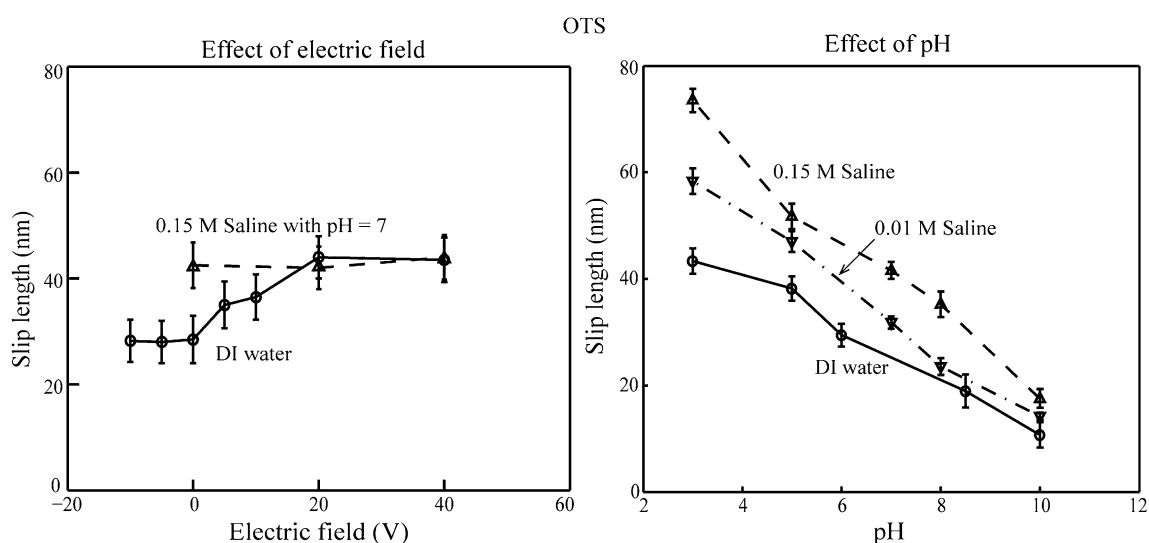
Fig. 6 Effect of applied voltage and pH on the slip length on OTS surfaces immersed in 0.01 and 0.15 M saline solutions and DI water (adapted from Jing and Bhushan, 2013b)

where b is the slip length considering surface charge, b_0 is the slip length without considering surface charge, α is a numerical factor, σ is the surface charge density, d is the equilibrium distance of Lennard–Jones potential, e is the elementary charge, and l_B is the Bjerrum length. The existence of surface charge at the solid–liquid interface will generate an attractive electrostatic force between the solid and liquid, enhance the interaction between the solid and liquid, and reduce the slip length. Here, the decreasing electrostatic force applied on the AFM probe with increasing applied voltage means a decreasing magnitude of surface charge density at the solid–liquid interface. This leads to an increase in the slip length with the increasing applied voltage (Li and Bhushan 2015).

Figure 7b shows the slip length data as a function of applied voltage values for three superhydrophobic surfaces with different degrees of oleophobicity immersed in DI water, hexadecane and ethylene glycol. The slip length in the case of DI water increases with an applied electric field from 0 to 60 V. The slip lengths in the cases of hexadecane and ethylene glycol does not change with an applied electric field value from 0 to 70 V. The measured slip lengths of the superhydrophobic/oleophobic surface in DI water, hexadecane, and ethylene glycol are larger than those of the superhydrophobic/superoleophilic surface. The changes of slip lengths of the superhydrophobic/superoleophilic surface and the superhydrophobic/superoleophobic surface in DI water, hexadecane, and ethylene glycol with an applied voltage are similar to those of the superhydrophobic/superoleophilic surface. It should be noted that, in the case of the superhydrophobic/superoleophobic surface, the error range of the measured value of slip length is larger than that on the other two superhydrophobic surfaces. This can be explained by the higher RMS and P–V distance of the superhydrophobic/superoleophobic surface. The measured slip length is different at the point of the peak than that of the valley on the surfaces, which induces the larger error range of slip measurement.

Figure 8a shows the measured slip length data for PS and OTS surfaces immersed in DI water and ethylene glycol as a function of pH values (Li and Bhushan 2015). For PS immersed in DI water with different pH values, the slip length decreases with the increasing pH value from 3 to 7, and remains constant with the increasing pH value from 7 to 11. For the OTS surface, the slip length decreases with the increasing pH value from 3 to 11. The OTS and PS surfaces immersed in DI water are believed to be negatively charged. When the pH value increases, the increasing concentration of OH⁻ increases the absolute value of negative charge at the interface. Based on the theoretical study by Joly et al. (2006) an increase in the surface charge will

result in a decrease of the slip length, which is in agreement with this experimental result.

For the PS immersed in ethylene glycol with different pH values, the slip length increases when the pH value increases from 3 to 8, then decreases when the pH value increases from 8 to 11. Similar results can be obtained on the OTS surface. The OTS and PS surfaces immersed in ethylene glycol are also negatively charged by the adsorption of OH⁻ at the interface. However, the surface charge density is smaller than that in DI water. When the pH value of ethylene glycol changes from 8 to 3, the increasing concentration of H⁺ may reduce the negative surface charge to zero at the very beginning. Then, with a further increase of the concentration of H⁺ the surface will be subjected to an increasing positive charge. This results in the decrease of slip length when the pH value decreases from 8 to 3. When the pH value increases from 8 to 11, the increasing concentration of OH⁻ promotes the adsorption of OH⁻ at the interface, and this increases the absolute value of negative surface charge and, therefore, leads to the decrease of slip length.

Figure 8b shows the measured slip length data of the superhydrophobic/superoleophilic, superhydrophobic/oleophobic, and superhydrophobic/superoleophobic surfaces immersed in DI water and ethylene glycol as a function of pH values. For the superhydrophobic/superoleophilic surface immersed in DI water with different pH values, slip length decreases with the increasing pH from 3 to 11. Similar results can be obtained on the other two surfaces. The mechanisms of the change in slip length can still be explained by the effect of pH on the surface charge density at the interface. The three surfaces are also believed to be negatively charged in DI water with the dissociation of the silanol group. The change in pH will affect the dissociation of the silanol group, the surface charge density, and causes a change in the slip length.

A schematic of the surface charge on the three surfaces immersed in ethylene glycol is shown in Fig. 9 (Li and Bhushan 2015). When the pH value decreases from 8 to 3, the increasing concentration of OH⁻ promotes the dissociation of the silanol group and increases the absolute value of the negative charge at the interface. This leads to the decrease of slip length according to Eq. (7). For the superhydrophobic/superoleophilic surface immersed in ethylene glycol with different pH values, slip length increases when the pH value increases from 3 to 8, then decreases when the pH value increases from 8 to 11. It is believed that when the pH value of ethylene glycol is equal to 8, the negative surface charge density is small, and when the pH value decreases, the surface will be subject to a positive charge. Then, when the pH value changes from 8 to 3 or 8–11, the

Effect of electric field
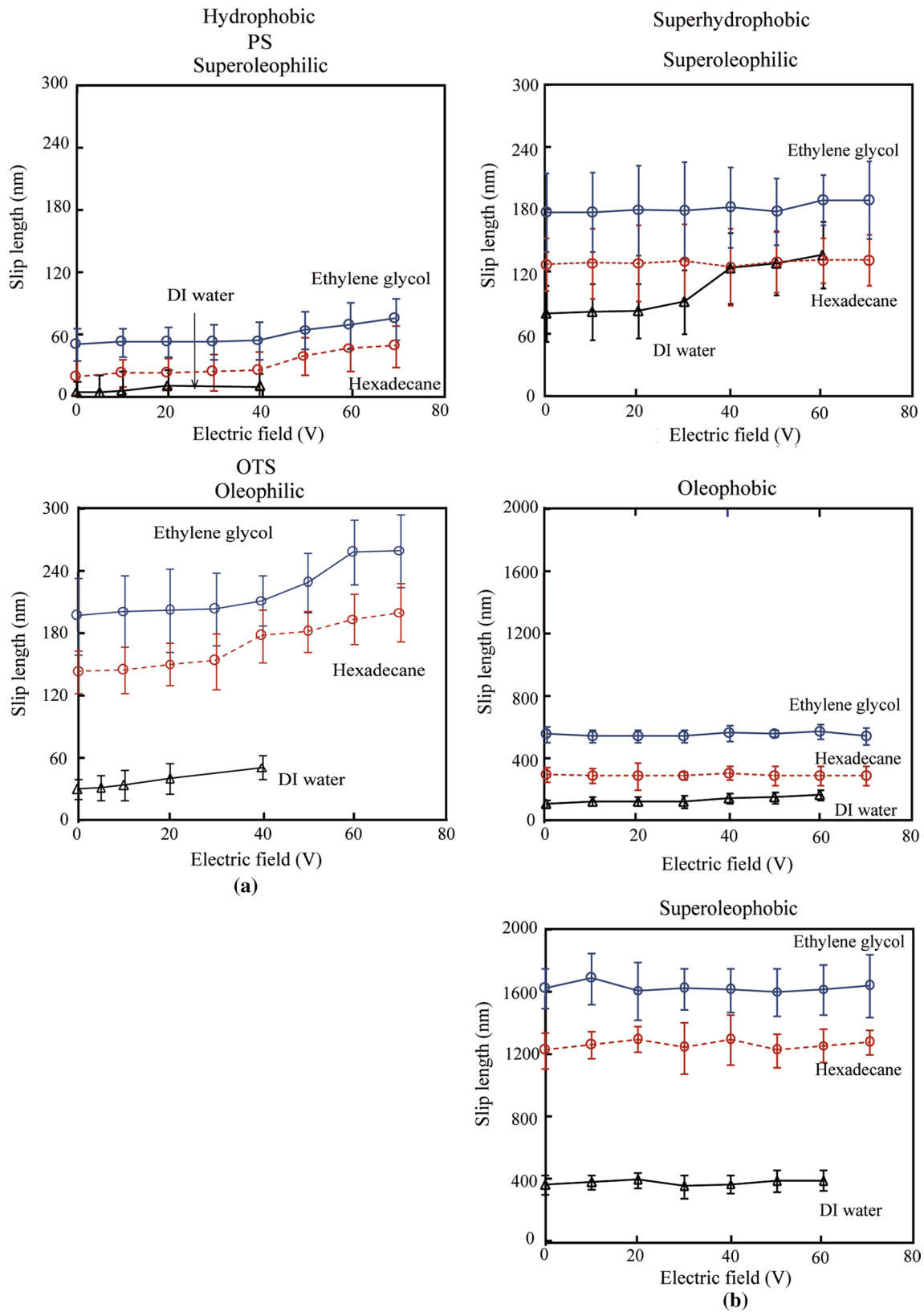
(a)

(b)

increasing concentration of H^+ or OH^- will increase the absolute value of the positive or negative charge, leading to a decrease of slip length.

4 Generation of nanobubbles on hydrophobic surfaces

Nanobubbles are soft gas domains that form on the solid–liquid interface. They can be formed spontaneously on smooth hydrophobic surfaces. At high surface roughness, either nanobubbles cannot be imaged or are not formed. Their size ranges from few nm to several microns. Nanobubbles are believed to be partly responsible for boundary slip and reduction of drag at the solid–liquid interface (Wang and Bhushan 2010; Maali and Bhushan 2013; Li et al. 2016).

The tapping mode AFM images of hydrophilic mica surface and hydrophobic (with n-hexatriacontane wax layer) samples at two loads (95 and 85% set points) are shown in Fig. 10 (Wang et al. 2009a). A featureless image was obtained on the hydrophilic mica surface at two loads. However, for the hydrophobic surface near spherical objects (nanobubbles) were observed over whole area. The diameter and height of the nanobubbles at 95% set point was 150 and 6 nm, respectively. At higher load (85% set point), nanobubbles coalesced and larger nanobubbles with lower density were observed. Nanobubbles were found to be stable at the same scanning conditions for several hours.

In studying formation of nanobubbles on the variety of surfaces, micropancakes have also been discovered (Zhang et al. 2007; Seddon and Lohse 2011; Li et al. 2016). These consist of a very thin film of gas having a height of a few nm and very wide, up to a few μm.

4.1 Role of nanobubbles on fluid slip and drag

The role of nanobubbles on slip length (Tretheway and Meinhart 2004; Wang et al. 2009a; Maali and Bhushan 2013; Li et al. 2016) and drag (Maali and Bhushan 2013) has been investigated. To understand the role of nanobubbles on slip length, Tretheway and Meinhart (2004) calculated the slip length for the fluid flow between two infinite parallel plates by modeling the presence of either a

depleted water layer or nanobubbles as an effective air gap at the wall. They reported that the slip length increases with an increasing value of air gap thickness, assuming that air covers the wall continuously. For an intermittent surface coverage of nanobubbles, the slip length increases with increasing nanobubble height and surface fraction covered by nanobubbles. A schematic of nanobubbles and velocity profiles presented in Fig. 11, shows the impact on boundary slip in squeeze experiments, where h_b is an effective thickness of the air gap induced by nanobubbles (Wang et al. 2009a). When a gas layer exists between a solid surface and a liquid, the slip length generated by the discontinuity of viscosity at the liquid–gas interface is give as (Vinagradova 1995),

$$b = \left(\frac{\eta_w}{\eta_a} - 1 \right) h_b \tag{8}$$

The viscosities for water and air at a temperature of 300 K are about $\eta_w = 851.5$ μPa s and $\eta_a = 18.6$ μPa s, respectively (Haynes 2014). Therefore, slip length b may be lead to about 45 times air gap thickness h_b due to high value of η_w/η_a.

Li et al. (2016) measured slip length and geometrical distribution of nanobubbles on various PS surfaces. To obtain surfaces with different nanobubble coverage, PS surfaces with different surface roughness were immersed in partially degassed DI water or air-equilibrated DI water. Gas concentration in water has an important effect on the formation of nanobubbles to be discussed later (Khasnavis et al. 2012; Bhushan et al. 2013). Different surface roughness of PS surfaces were obtained by changing the concentration of PS solution. Surface roughness, geometrical data of nanobubbles and slip data are presented in Table 4. The data shows that slip length increases with an increase in the size (diameter and height), surface coverage of nanobubbles, and decrease in the contact angle of nanobubbles. The data suggests that nanobubbles act as a lubricant and increase the slip length. Modeling suggests that an increase in the slip is expected to increase fluid flow with lower fluid drag (Jing and Bhushan 2013c).
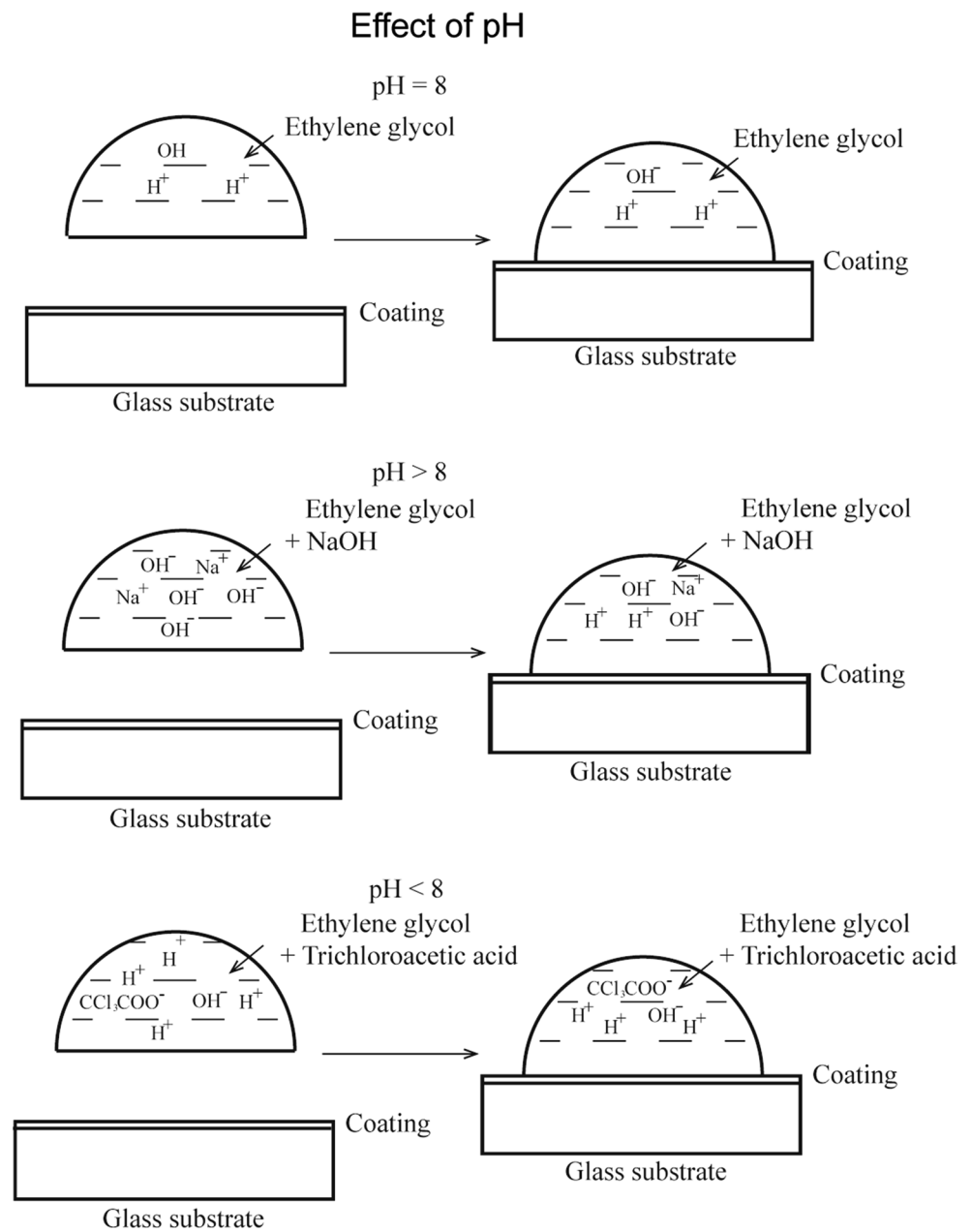
4.2 Coalescence and stability of nanobubbles

Due to their high Laplace pressure, nanobubbles should disappear after a few seconds. However, studies have shown that nanobubbles can exist for several hours (Yang et al. 2003) or even days (Craig 2011), and are stable at temperatures ranging from 30 to 50 °C (Seddon et al. 2011), under water pressure to −6 MPa (Borkent et al. 2007) and under aggressive mechanical agitation (Bhushan et al. 2009; Wang and Bhushan 2010). Bhushan et al. (2008) studied coalescence and stability of nanobubbles on hydrophobic
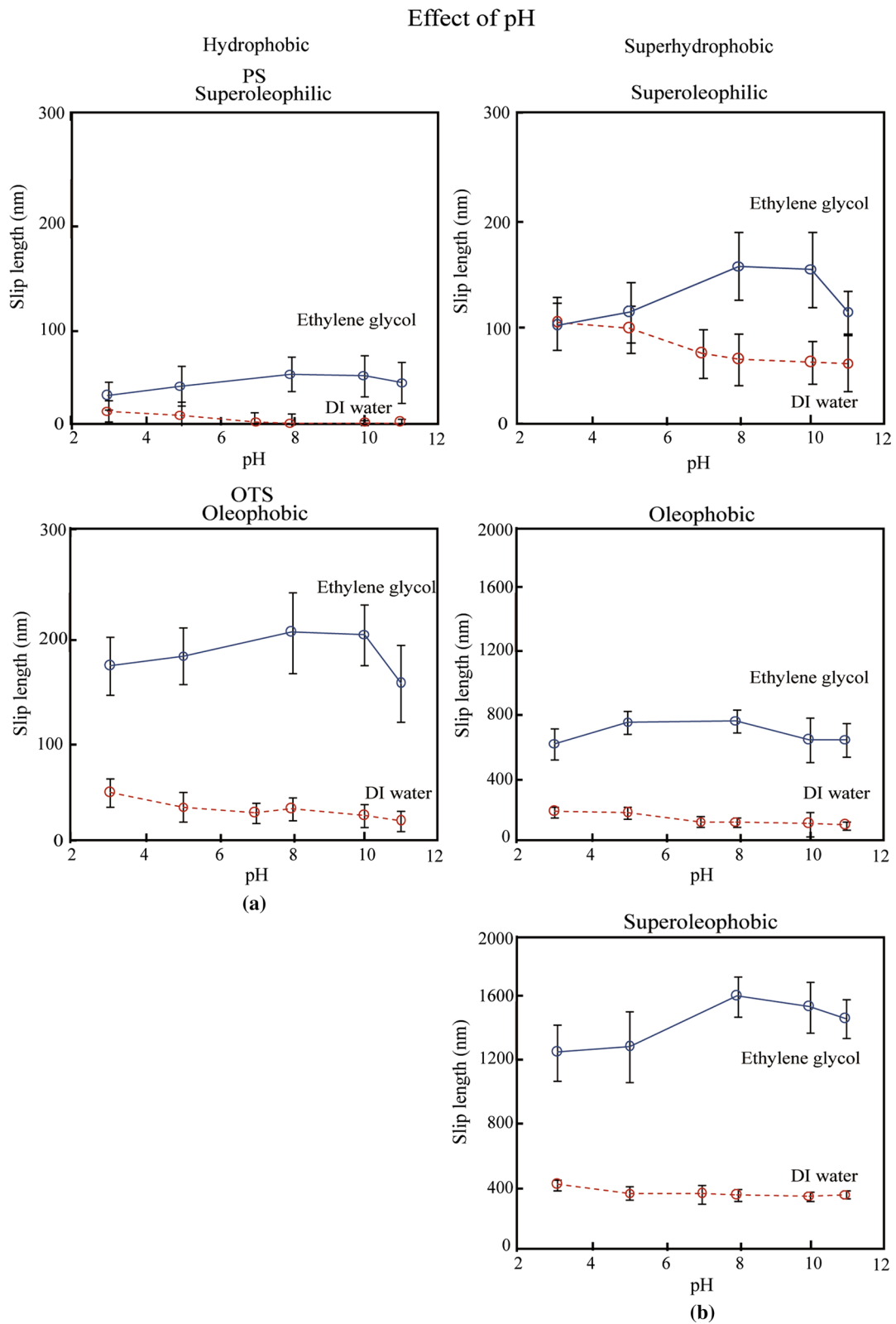
Fig. 8 Measured slip length of **a** two hydrophobic surfaces and **b** three superhydrophobic surfaces immersed in DI water and ethylene glycol with different pH values (adapted from Li and Bhushan 2015)
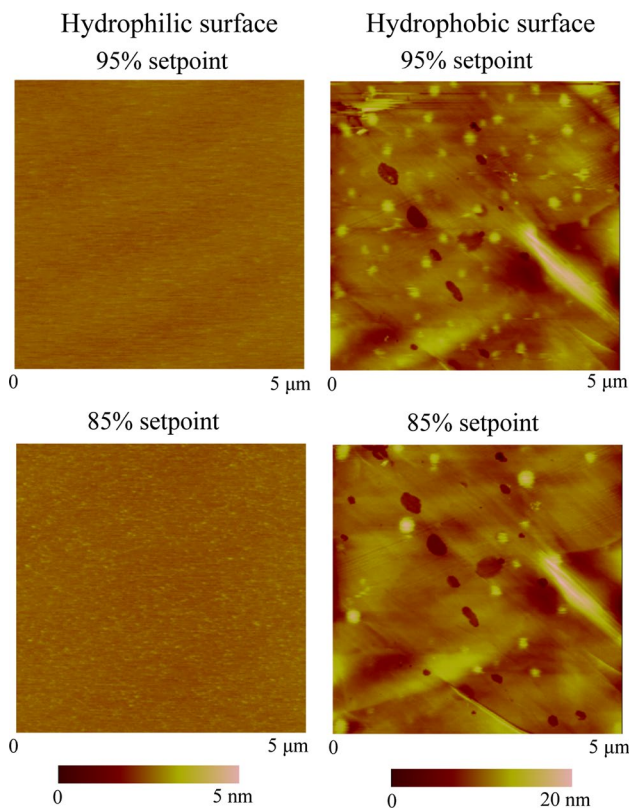
polystyrene coated silicon wafer in DI water during scanning with AFM.

By performing AFM imaging in tapping mode in air, a featureless image of the original PS coated silicon wafer surface was obtained, as shown in Fig. 12a. The RMS roughness and peak-to-valley distance R_{max} are 0.21 and 2.3 nm, respectively. Figure 12b shows the image of PS surface immersed in DI water. The entire surface is covered with spherical cap like domains. The diameter and height of these caps are generally on the order of 200 nm and 20 nm, respectively. The RMS roughness and R_{max} are 8.2 and 69 nm, respectively, which are about two orders of magnitude larger than that obtained in air. Some large domains are observed in the vicinity where nanobubble density is lower than that at other places. That is expected to be a result of local nanobubble coalescence (Bhushan et al. 2008).

Figure 13 shows the effect of scan speed and scan load on propensity of nanobubbles (Bhushan et al. 2008). Figure 13a (left) was obtained at 95% setpoint and full $5\mu m$ μm × 5 μm area scan. Then the central 2 μm × 2 μm area scan was performed two times with the same 95% amplitude setpoint. After that, the 5 μm × 5 μm area scan was imaged again with 95% setpoint to obtain the

Hydrophilic surface
95% setpoint

Hydrophobic surface
95% setpoint

0   5 μm   0   5 μm

85% setpoint

85% setpoint

0   5 μm   0   5 μm

0   5 nm   0   20 nm

Fig. 10 Tapping mode AFM images of hydrophilic (mica) and hydrophobic (mica coated with wax layer) surfaces in DI water with 95 and 85% setpoint of free amplitude, corresponding to about 0.09 and 0.26 nN normal forces, respectively. Nanobubbles with typical diameter of 150 nm were observed on the hydrophobic surface. Nanobubble coalescence was observed on the hydrophobic surface after high load scanning (Wang et al. 2009a)

Sphere

Liquid

Velocity profile

z

x

Nanobubbles

H_b h_b Hydrophobic substrate
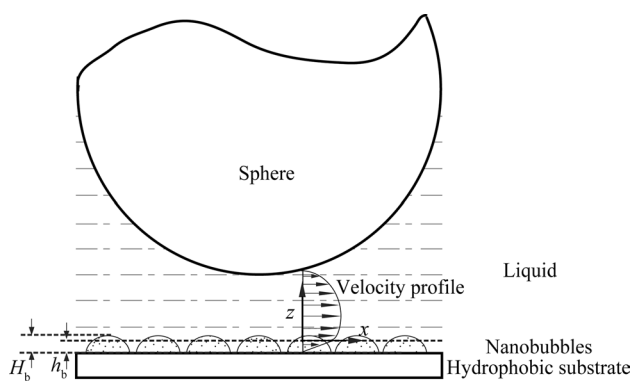
Fig. 11 Schematic of a sphere being squeezed on a flat surface, with nanobubbles distributed on the flat surface. The presence of nanobubbles on the flat surface changes the velocity profile between the sphere and the plane surface, which results in an increase of slip length. The nanobubbles with a height H_b can be approximated by a gas layer with effective thickness h_b (Wang et al. 2009a)

images shown in Fig. 13a (right). One can find larger nanobubbles generated in the central area with lower density. The diameter and height of the nanobubbles increase to 420 and 55 nm, respectively, in Fig. 13a. Therefore, some nanobubbles must have coalesced and generated larger ones. The only difference between the 2 μm × 2 μm central area scan of Fig. 13a (right) and (left) images is the scan speed. When working at the same scan rate, the scan speed of the 5 μm × 5 μm area scan is one-and-a-half times higher than that in the 2 μm × 2 μm area scan. Assuming the power transferred from the cantilever tip to sample surfaces is constant during the test, the low speed implies higher power transfer at the same scan area than at high scan speed, and nanobubbles suffer more disturbance. Therefore, the coalescence occurred even with the same setpoint of amplitude.

In addition to scan speed, scan load also affects nanobubble imaging (Bhushan et al. 2008). The sample scanned after the two scan speeds in Fig. 13a was used for scan load studies. After, applying 90% setpoint scan to the whole 5 μm × 5 μm area of Fig. 13a (right), a 95% setpoint scan was performed in the full area, and nanobubble images with a lower density were obtained, as shown in Fig. 13b (left). Nanobubble density is reduced while nanobubble size abruptly increases with the normal diameter over 550 nm and height over 77 nm. With lower nanobubble density, it is possible to track coalescence of nanobubbles. In the central area containing six numbered nanbubbles of Fig. 13b (left), central 2 μm × 2 μm area scan was performed two times with 90% setpoint. After that, 95% setpoint scan was performed over the full area, and a further nanobubble coalescence image was obtained, as shown in Fig. 13b (right), where the diameter and height of nanobubbles increased from 550, and 77 up to 690 and 100 nm, respectively (Bhushan et al. 2008).

By comparing Fig. 13b (left with right), one can find that, except for the six numbered nanobubbles in the left, the sizes and locations of other nanobubbles remained unchanged in Fig. 13b (right). Based on their location, nanobubbles b1, b2, and b3 were believed to coalesce and generate the larger nanobubble b7. Similarly, b4, b5, and b6 joined together and formed nanobubble b8. One can find that during nanobubble coalescence, small nanobubbles (b1, b3 and b5, as well as b6) tend to move first and coalesce with b2 and b4, generating larger nanobubbles. This should be because the large nanbubbles have a strong interaction with surface due to their long length of contact line with the surface (Bhushan, et al. 2008).

To verify nanobubble coalescence, Bhushan et al. (2008) calculated the quantity of gas molecules trapped in the nanobubbles before and after scanning at high load. They used the Laplace pressure multiplied by the volume of nanobubbles

Table 4 Geometrical data of nanobubbles on PS films with different surface roughness immersed in partially degassed DI water or air-equilibrated DI water and the slip length measured on corresponding substrates (Li et al. 2016)

PS substrate	RMS roughness (nm)	Average diameter (nm)	Average height (nm)	Coverage rate (%)	Average contact angle[a] (°)	Average slip length (nm)
1	0.86 ± 0.02	78	15.3	1.7	42.8	8 ± 2.4
2	1.05 ± 0.03	157	21.6	4.8	30.8	21 ± 3.2
3	1.87 ± 0.05	332	35.6	15.5	24.2	85 ± 6.3
4	2.16 ± 0.06	451	44.8	50.8	16.6	512 ± 27.6

[a] The contact angle was obtained through gas side of nanobubbles
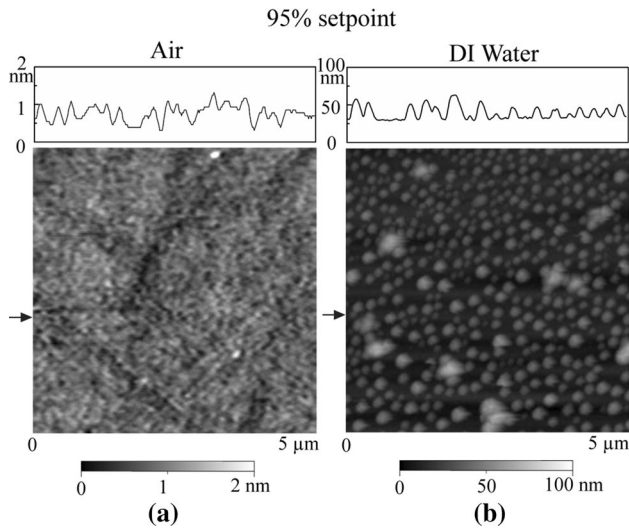
Fig. 12 Tapping mode AFM images of polystyrene coated silicon wafers in **a** air and **b** DI water. Section profiles are taken at locations shown by *arrows* in AFM images (adapted from Bhushan et al. 2008)

as a measure of the quantity of gas molecules. They found that the volume of nanobubble b7 was approximately equal to the total volume of nanobubbles b1, b2, and b3.

To summarize, nanobubbles are found to be very sensitive to scan parameters while imaging and coalescence occurs after scanning. To obtain nanobubble images without movement and coalescence, a higher setpoint (corresponding to lower scan load), higher scan rate, and larger scan area are desirable. At high load and low scan speed, the nanobubbles will be coalesced or moved during the imaging load, and in some cases cannot be observed.

4.3 Nanobubble-substrate interaction

Physical interaction of nanobubbles with polymer films in the presence of nanobubbles was studied by Wang et al. (2009b). Nanobubble induced nanoindents on ultrathin PS films in DI water was reported. A time-series imaging was

performed to study the evolution of nanoindents on PS surface in water.

Before immersion in DI water, the surface of the PS film was observed to be uniform and smooth with an RMS roughness of about 0.22 nm (Fig. 14a). After being immersed in water for 10 min, the PS surface was imaged and nanobubbles were observed to emerge on the surface (Fig. 14b) (Wang et al. 2009b). In Fig. 14, the section profiles were taken at positions shown by arrows in AFM images and show structures of sample surface and nanobubbles. The roughness increased to 1.3 nm, which is significantly larger than that in air. The nanobubbles on the substrate were not uniform in their size and were distributed around two peaks. The large nanobubbles had a diameter of around 100 nm and a height of around 6 nm. The small nanobubbles had a diameter of around 50 nm and a height of around 1.5 nm. The densities for the small and large nanobubbles were estimated to be about 2.0×10^8 and $0.68 \times 10^8/mm^2$, respectively. The diversity of the nanobubble size appeared to be related to the heterogeneous surface property of the PS film, in particular, the roughness. It has been reported that nanobubbles on a rough surface are much less densely populated, and their sizes are relatively larger than those on a smooth surface (Wang and Bhushan 2010).

Sequence of nanobubble height images of the PS sample immersed in DI water, as a function of immersion time, for the duration of several hours are shown in Fig. 15 (Wang et al. 2009b). The section profiles were taken at positions shown by arrows in AFM images. It is clear that the morphologies of the nanobubbles and the PS surface experienced continuous change in time. After 10 min, spherical nanobubbles with smooth profiles were observed, which can be observed in the section profile of Fig. 15a. After 40 min, both small nanobubbles and large nanobubbles appear to shrink in size. Most distinctly, circular rims emerged at the perimeter of large nanobubbles, which also can be seen from the section profile (Fig. 15b). Typical height of the rim is about 1 nm. After 150 min, the typical height of rims increased to about

Scan speed influence

(a)

Scan load influence

(b)
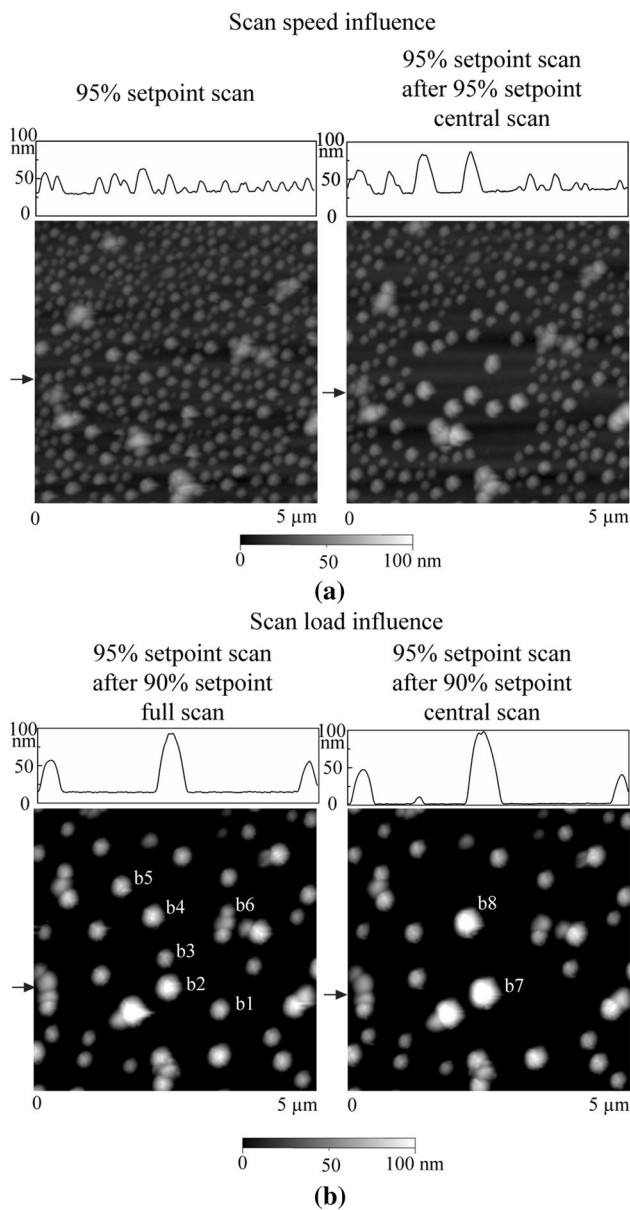
Fig. 13 Sequence of nanobubble images obtained in the same 5 μm × 5 μm scan area with **a** 95% amplitude setpoint scan (*left*) and 95% amplitude setpoint scan preceded by scanning with 95% amplitude setpoint in central 2 μm × 2 μm area for two times (*right*). Nanobubble coalescence is observed with lower scan speed in the central area (*right*), **b** 95% amplitude setpoint scan preceded by scanning with 90% amplitude setpoint in full 5 μm × 5 μm scan area (*left*) and 95% amplitude setpoint scan preceded by scanning with 90% amplitude setpoint in central 2 μm × 2 μm area for two times (*right*). Further coalescence of nanobubbles is observed at higher scan load, Fig. 13b. Section profiles are taken at locations shown by *arrows* in AFM images (Bhushan et al. 2008)

2 nm (Fig. 15c). Most of the small nanobubbles disappeared in Fig. 15c, leaving small nanoindents at their original positions with a diameter of about 20 nm.
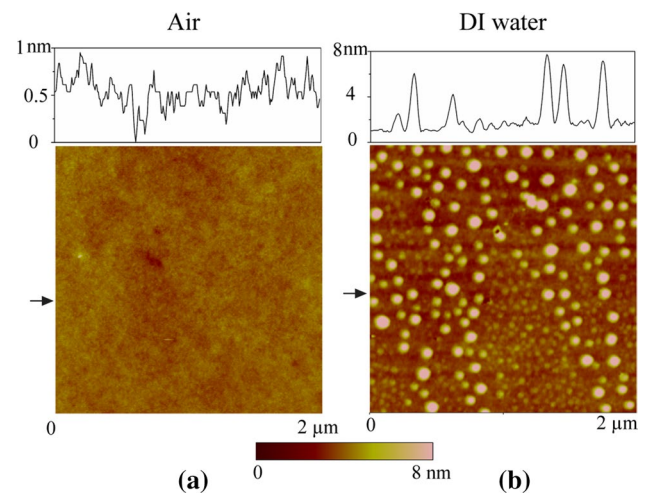

Fig. 14 Comparison of images of polystyrene samples using tapping mode AFM in **a** air and **b** DI water. Two groups of different sizes of nanobubbles can be observed. The section profiles are taken at positions shown by *arrows* in AFM images and show structures of sample surface and nanobubbles (adapted from Wang et al. 2009b)

One nanoindent is pointed out by an arrow in Fig. 15c as an example. After 225 min, another scan area was chosen to exclude the possibility of cantilever tip influence on the evolution of nanobubbles and formations of nanoindents. All of the small nanobubbles disappeared and left densely distributed nanoindents. However, larger nanobubbles were still present on the surface.

Three dimensional images for a nanobubble circled in Fig. 15 after 10 and 150 min was given in Fig. 16 to illustrate the topography change (Wang et al. 2009b). At the time of 10 min, the nanobubble had a smooth profile. However, a rim appeared around the nanobubble at the time of 150 min, the diameter of the nanobubble slightly shrank after appearance of the rim.

Wang et al. (2009b) reported that a strong correlation exists between the presence of nanobubbles and nanoindents which suggests that nanobubbles can induce nanoindents. They suggested that high inner Laplace pressure and surface tension force due to the three phase contact line increases the instability of PS surface near nanobubbles. For typical nanobubbles that were measured, calculated inner pressure was on the order of 2 MPa. This high inner pressure with respect to the ambient pressure outside the nanobubbles would squeeze PS chains, contributing to the formation of rims around nanobubbles. The horizontal component of the total surface tension force along the contact line and inner pressure are believed to be responsible for the formation of nanoindents on the site of nanobubbles. Nanoindentation experiments on PS surfaces by indenting it with an AFM tip at a contact pressure of about 50 MPa, demonstrated the formation of nanoindents.

Immersed in DI water
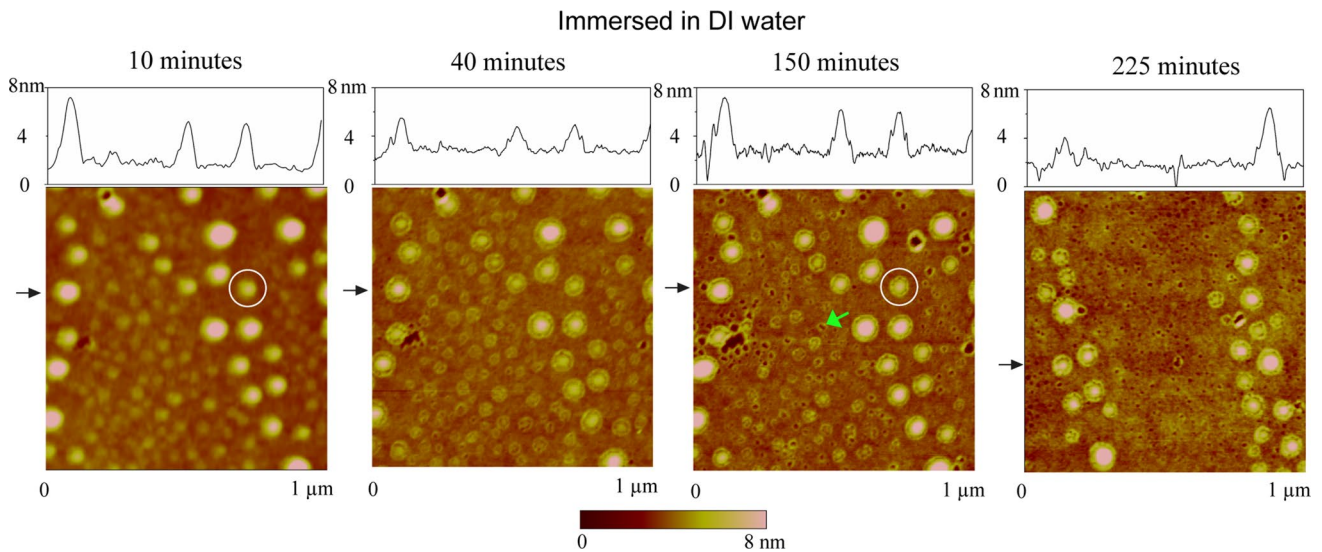
Fig. 15 Sequence of nanobubble height images as a function of time of polystyrene samples immersed in DI water in 1 μm × 1 μm scan area after 10, 40, 150, and 225 min. Rims appear after 40 min. Small nanobubbles gradually disappear, leaving nanoindents at corresponding sites, one of which is pointed out by an *arrow* after 150 min and finally small nanobubbles disappear after 225 min. The section profiles are taken at positions shown by *arrows* in AFM images. From section profiles, one can see that rims appear after 40 min and gradually grow up with immersion time. *White circles* in the first and third images are used to show rim structures in the following figure through 3D images (adapted from Wang et al. 2009b)

Immersed in DI water
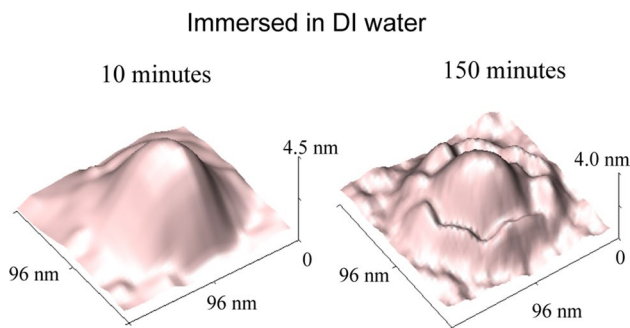
Fig. 16 3D images of a nanobubbles circled in Fig. 15 after 10 and 150 min the polystrene sample was immersed into DI water. The profile of the nanobubble is smooth at 10 min and a rim appeared around the nanobubble at 150 min (adapted from Wang et al. 2009b)

4.4 Effect of electric field and liquid pH values on propensity of nanobubbles

Mazumder and Bhushan (2011) studied the effect of electric field and liquid pH on propensity of nanobubbles on a polystyrene surface in DI water and saline solutions. The pH of DI water and saline solution was measured to be 7.0 ± 0.1 each. The target pH of 3.4 ± 0.1 and 10 ± 0.1 was achieved by adding 0.01 M HCl and 0.01 M NaOH, respectively to both liquids. Figures 17 and 18 show the AFM images and histograms of size distribution of nanobubbles immersed in DI water and saline solution, respectively, with positive and negative voltage applied to the silicon substrate with respect to the liquid. Geometrical distribution of nanobubbles are presented in Fig. 19. In both DI water and saline solution, when an increasing positive bias is applied, the percent area covered and average diameter of nanobubbles increase, and the total count decreases. However, the distribution of nanobubbles is largely unaffected on application of negative substrate voltage.

The limited effect seen when the substrate was negatively biased was attributed to the following by Mazumder and Bhushan (2011). Due to the presence of the insulating silicon oxide and PS layers, there forms a gradient of differential charging across the insulating layers. The extent of charging across the two insulating layers varies depending on whether the substrate is positively or negatively biased. This is possibly caused by the interfacial charges at the substrate/oxide, oxide/PS and PS/liquid interfaces. They believed that differential charging occurs at the above interfaces causing a difference in the effective net voltage at the PS/water surface even when the voltage applied by the external power supply remains the same. The effective net voltage is significantly small when the substrate is negatively biased with respect to the electrode in the liquid.

Figure 20 shows the AFM images and histograms of size distribution of nanobubbles immersed in DI water and saline water with three pH values. Figure 21 shows the geometrical distribution of nanobubbles. The results show that
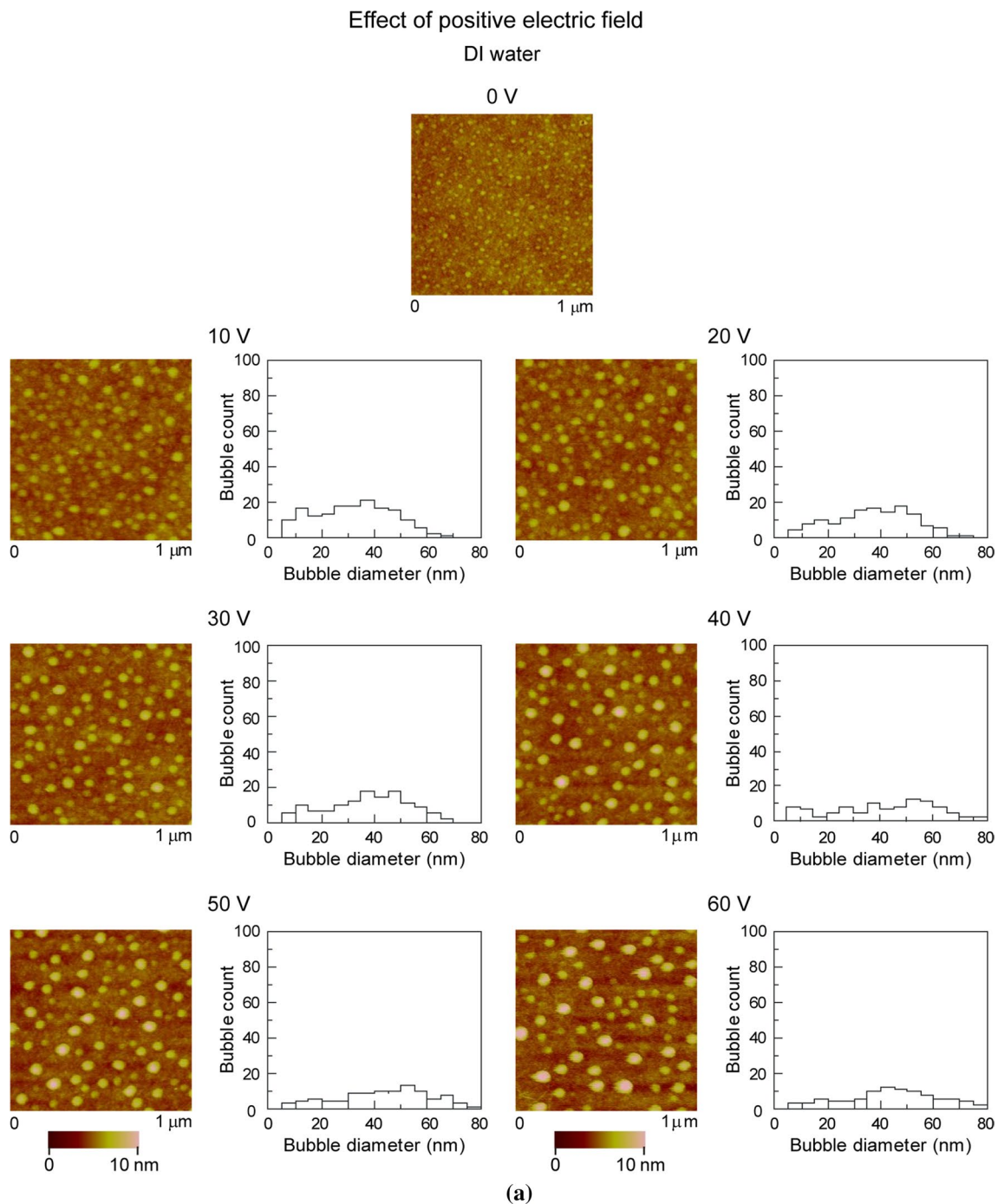
Fig. 17 AFM images and the corresponding histograms of the size distribution of nanobubbles on the polystyrene film in DI water for a series of **a** positive and **b** negative potential applied to the substrate (adapted from Mazumder and Bhushan 2011)

for both DI water and saline solution, as the pH increases from 3.4 to 10.1, the percent area covered, total count and average diameter of nanobubbles increase. In the case of saline solution, the increase in the size of nanobubbles is more pronounced at higher pH values (Mazumder and Bhushan 2011).

4.5 Applications of speciality fluids with nanobubbles in biomedicine

Nanobubbles in fluids have gained some interest due to their wide range of applications in biology, medicine, and engineering. As an example, nanobubbles can be used as a
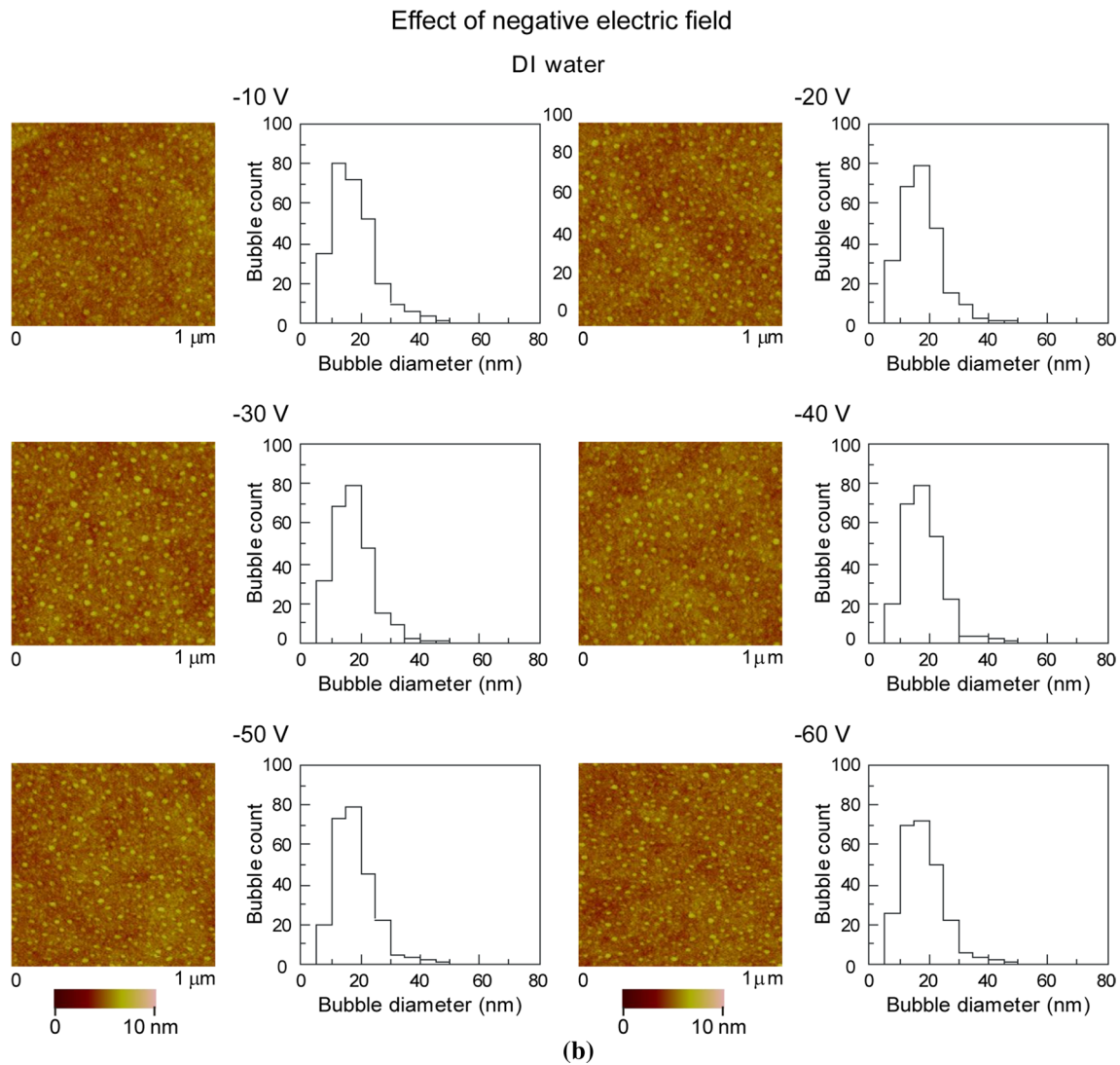
Fig. 17 continued

vehicle for drug delivery and as contrast agents for imaging and drug monitoring (Khasnavis et al. 2012). Specifically, nanobubbles produced using oxygenated fluid have promising applications in environmental and medical treatment. The flow chart in Fig. 22a lists some applications of oxygenated nanobubbles (Bhushan et al. 2013). In the case of waste water treatment, nanobubbles have been employed in the detoxificaton of water and for degradation of organic compounds in water. In medical treatment, nanobubbles containing oxygen have been used as contrast agents, as an approach for targeted oxygen release to treat inflammation and for thrombosis. As an example, Fig. 22b shows transmission electron microscopy (TEM) images of oxygenated micro/nanobubbles applied to wastewater treatment. In this study by Uchida et al. (2011), oxygenated nanobubbles were used to capture impurities found in polluted wastewater.

Although inflammation is a protective cellular response aimed at removing injurious stimuli and initiating the healing process, prolonged inflammation, known as chronic inflammation, goes beyond physiological control. Some experimental oxygenated and electrokinetically altered oxygenated fluids have been developed to inhibit inflammation (Khasnavis et al. 2012).

An experimental electrokinetically altered oxygenated fluid (RNS60, Revalesio Corp., Tacoma, Washington) is a physically modified saline that is generated by subjecting isotonic saline to controlled turbulence and Taylor–Couette–Poiseuille (TCP) flow under elevated oxygen pressure in a rotor/stator device. They have been found to inhibit the production of nitric oxide (NO) and the expression of inductible NO synthase in activated microglia. Inhibition of NF-KB activation by these solutions suggests that they exert the anti-inflammatory effect.
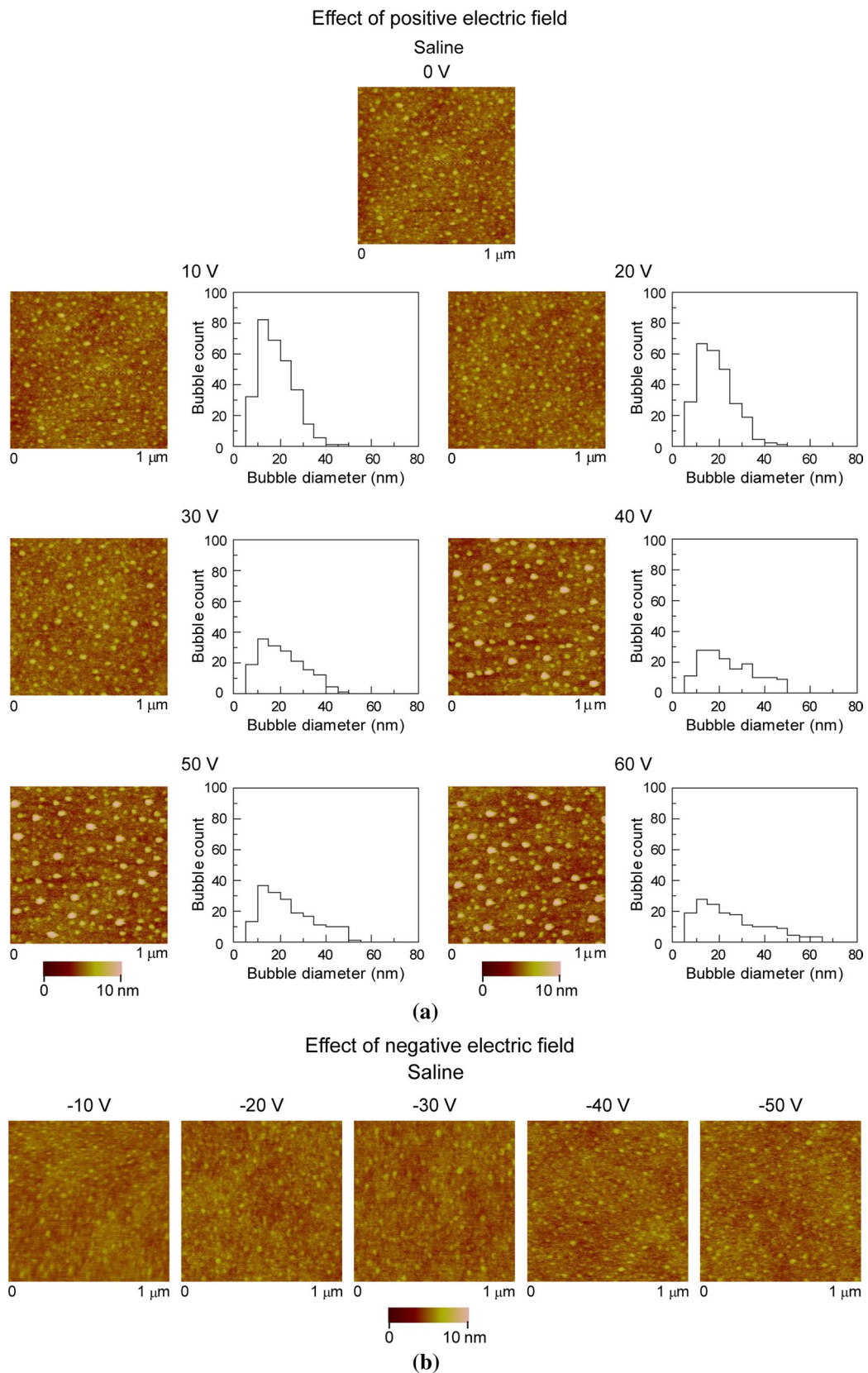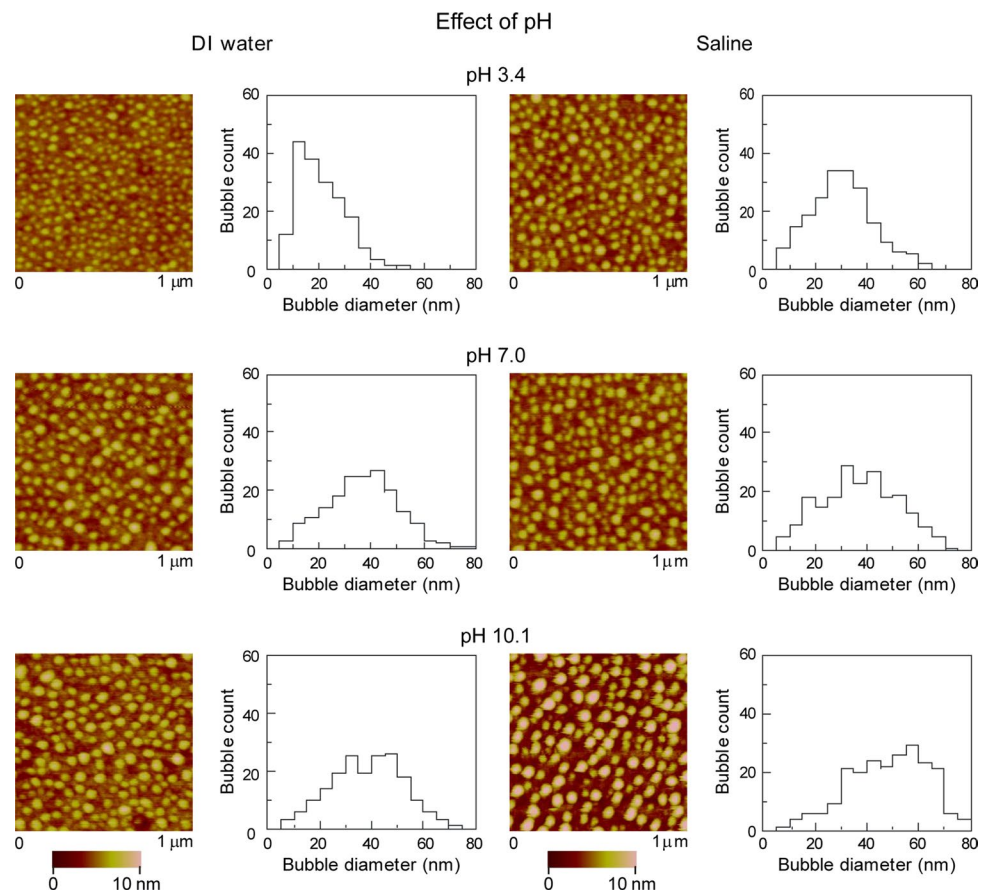
Fig. 18 AFM images and the corresponding histograms of the size distribution of nanobubbles on the polystyrene film in saline solution for a series of **a** positive and **b** negative potential applied to the substrate (adapted from Mazumder and Bhushan 2011)

Fig. 19 Geometrical distribution of nanobubbles on the polystyrene film in DI water (*top row*) and saline solution (*second row*) shown in Figs. 17 and 18, respectively. In DI water, the percent area covered and average diameter of nanobubbles increase and the total count of nanobubbles decreases with increasing positive potential applied to the silicon substrate. The distribution of nanobubbles is relatively unaffected in the range of negative potential. Similarly, in the case of saline solution the area covered and average diameter of nanobubbles increases and the total count of nanobubbles decreases with increasing positive potential applied to the silicon substrate (adapted from Mazumder and Bhushan 2011)
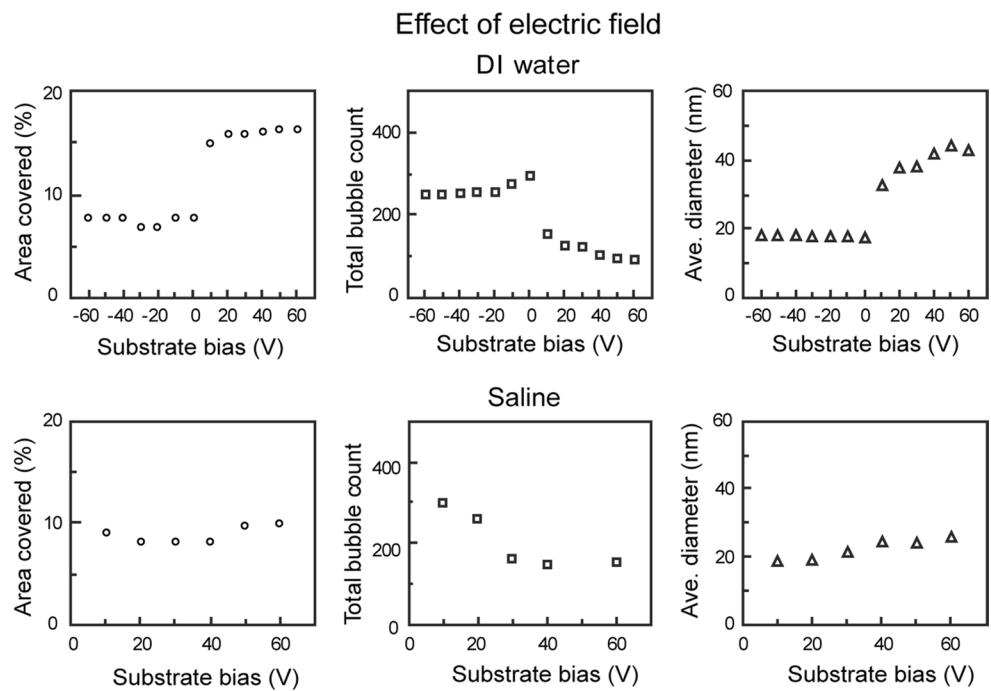
Fig. 20 AFM images and corresponding histograms of the size distribution of nanobubbles on the polystyrene film in DI water and saline water at pH 3.4, 7.0, and 10.1. The size of nanobubbles becomes larger at higher pH (adapted from Mazumder and Bhushan 2011)
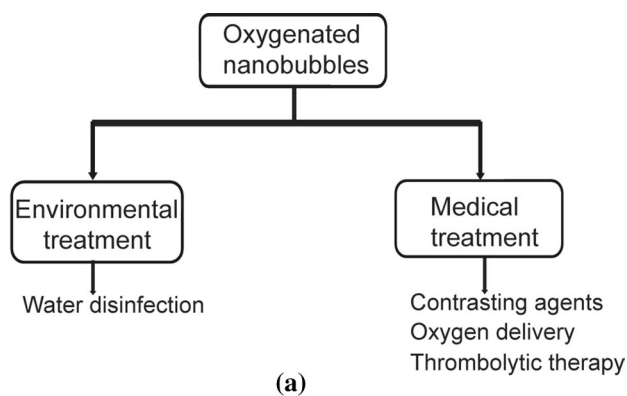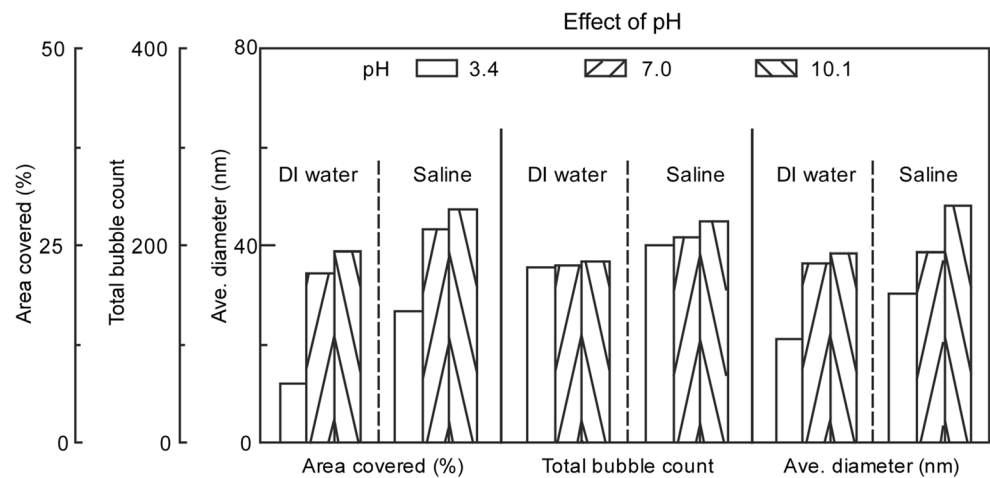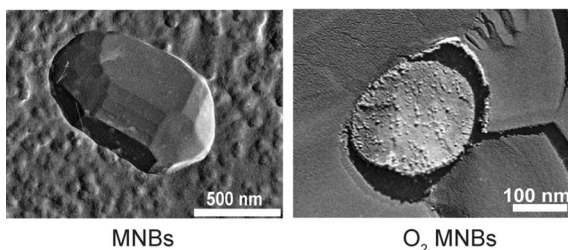
Fig. 22 a Flow chart showing some applications of oxygenated nanobubbles (Bhushan et al. 2013), and **b** an example of application of oxygenated nanobubbles in wastewater treatment (Uchida et al. 2011)

Knowledge of the size and density of nanobubbles produced in oxygenated fluid may lead to a better understanding of nanobubble formation and of their potential use in medical applications. Bhushan et al. (2013) measured morphology, size and density of nanobubbles formed on hydrophobic PS and octadecyltrichlorosilane (OTS) surfaces as well as slip condition in two experimental fluids-oxygenated and electrokinetically altered oxygenated fluid.

Oxygenated fluid (PNS60, Revalesio, Corp. Tacoma, Washington), referred to as saline 1 in this study, contained 0.9% saline containing excess oxygen (50–60 parts/million) and electrokinetically altered oxygenated fluid (RNS60, Revalesio, Corp. Tacoma, Washington), referred to as saline 2 in this study. The amount of dissolved oxygen in saline 2 was equivalent to that of saline 1. The studies of nanobubble formation in DI water and saline were used as a reference.

Representative data for nanobubbles in DI water, saline, oxygenated fluid and electrokinetically altered oxygenated fluid are shown in Fig. 23. Nanobubbles were instantaneously formed in all fluids. Oxygenated fluids produced larger size nanobubbles compared with DI water and saline. Between the two oxygenated fluids, electrokinetically altered oxygenated fluids produced the largest nanobubbles with larger area covered.

5 Closure

The reduction of fluid drag is of scientific interest in many fluid flow applications. Liquiphilic surfaces exhibit zero fluid slip at the liquid–solid interface, however liquiphobic surfaces are known to have fluid slip. The magnitude of the fluid slip is dependent upon the surface roughness of the solid, surface tension of the liquid, and degree of liquiphobicity. Surface charge, electric field, liquid pH, and gas concentration of the liquid affect the fluid slip. Nanobubbles can be formed on liquiphobic surfaces. A relationship between geometrical distribution of nanobubbles and fluid slip has been observed. The fluid slip facilitates fluid flow and is believed to result in lower fluid drag, of interest in many applications. Generation of nanobubbles can also be used for various biomedical applications.

Images and analyses of nanobubbles on PS surface in various fluids

(a)

(b)
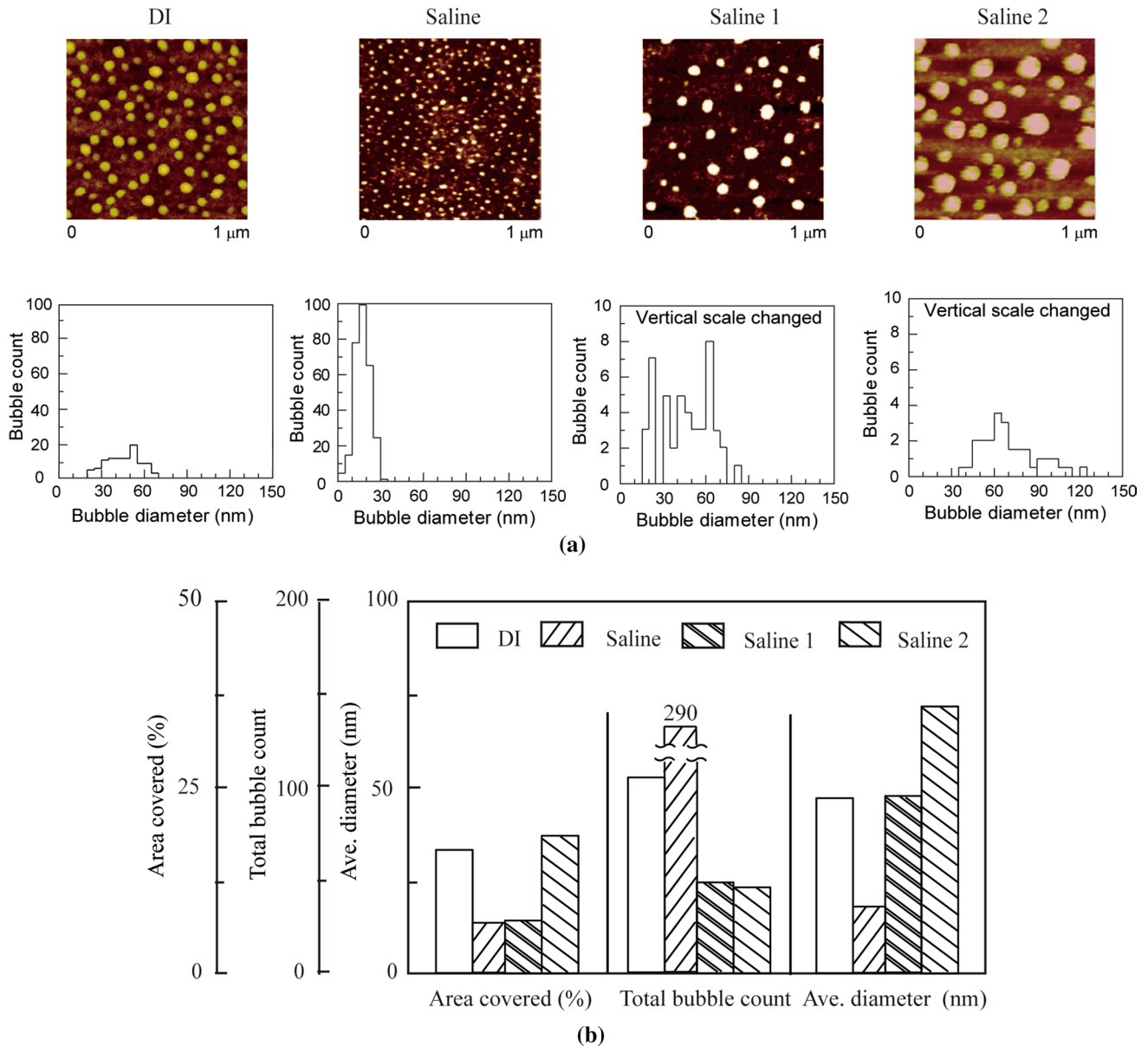
Fig. 23 AFM images of nanobubbles in DI water, saline 1, and saline 2 on a polystyrene surface imaged using tapping mode AFM. **a** Height images and corresponding histograms of geometrical distribution show the nanobubbles produced in oxygenated and electrokinetically altered fluids (saline 1 and saline 2) to be larger compared with DI water and saline. **b** Summary of the area covered, total count and average diameter of the nanobubbles data shown in **a**. Saline 1 and saline 2 show larger and fewer nanobubbles on the polystyrene film compared with DI water and saline (Bhushan et al. 2013)

References

Batchelor GK (1970) An introduction to fluid dynamics. Cambridge University Press, Cambridge

Bhushan B (2016) Encyclopedia of nanotechnology, 2nd edn, vol 1–6. Springer, Basel

Bhushan B (2017a) Springer handbook of nanotechnology, 4th edn. Springer, Basel

Bhushan B (2017b) Nanotribology and nanomechanics: an introduction, 4th edn. Springer, Basel

Bhushan B, Wang Y, Maali A (2008) Coalescence and movement of nanobubbles studied with tapping mode AFM and tip-bubble interaction analysis. J Phys Condens Matter 20:485004

Bhushan B, Wang Y, Maali A (2009) Boundary slip study on hydrophilic, hydrophobic, and superhydrophobic surfaces with dynamic atomic force microscopy. Langmuir 25:8117–8121

Bhushan B, Pan Y, Daniels S (2013) AFM Characterization of nanobubble formation and slip condition in oxygenated and electrokinetically altered fluids. J Colloid Interf Sci 392:105–116

Borkent BM, Dammer SM, Schoenher H, Vancso GJ, Lohse D (2007) Superstability of surface nanobubbles. Phys Rev Lett 98:204502–204506

Cottin-Bizonne C, Steinberger A, Cross B, Raccurt O, Charlaix E (2008) Nanohydrodynamics: the intrinsic flow boundary condition on smooth surfaces. Langmuir 24:1165–1172

Craig VSJ (2011) Very small bubbles at surfaces—the nanobubble puzzle. Soft Matter 7:40–48

Haynes WM (2014) CRC handbook of chemistry and physics, 95th edn. Taylor and Francis Group, Boca Raton

Jing D, Bhushan B (2013a) Boundary slip of superoleophilic, oleophobic, and superoleophobic surfaces immersed in deionized water, hexacadene, and ethylene glycol. Langmuir 29:14691–14700

Jing D, Bhushan B (2013b) Quantification of surface charge density and its effect on boundary slip. Langmuir 29:6953–6963

Jing D, Bhushan B (2013c) Effect of boundary slip and surface charge on the pressure-driven flow. J Colloid Interf Sci 392:15–26

Jing D, Bhushan B (2015) The coupling of surface charge and boundary slip at the solid–liquid interface and their combined effect on fluid drag: a review. J Colloid Interf Sci 454:152–179

Joly L, Ybert C, Trizac E, Bocquet L (2006) Liquid friction on charged surfaces: from hydrodynamic slippage to electroknietics. J Chem Phys 125:204716

Khasnavis S, Jana A, Roy A, Mazumder M, Bhushan B, Wood T, Ghosh S, Watson R, Pahan K (2012) Suppression of nuclear factor-κB activation and inflammation in microglia by physically modified saline. J Biol Chem 287:29529–29542

Li Y, Bhushan B (2015) The effect of surface charge on the boundary slip of various oleophilic/phobic surfaces immersed in liquids. Soft Matter 11:7680–7695

Li D, Jing D, Pan Y, Bhushan B, Zhao X (2016) Study on the relationship between boundary slip and nanobubbles on smooth hydrophobic surface. Langmuir 32:11287–11294

Maali A, Bhushan B (2008) Slip-length measurement of confined air flow using dynamic atomic force microscopy. Phys Rev E 78:027302

Maali A, Bhushan B (2012) Measurement of slip length on superhydrophobic surfaces. Philos Trans R Soc A 370:2304–2320

Maali A, Bhushan B (2013) Nanobubbles and their role in slip and drag. J Phys Condens Matter 25:184003

Maali A, Colin S, Bhushan B (2016) Slip length measurement of gas flow. Nanotechnology 27:374004

Mazumder M, Bhushan B (2011) Propensity and geometrical distribution of surface nanobubbles: effect of electrolyte, roughness, pH, and substrate bias. Soft Matter 7:9184–9196

Ou J, Perot B, Rothstein JP (2004) Laminar drag reduction in microchannels using ultrahydrophobic surfaces. Phys Fluids 16:4635–4643

Pan Y, Bhushan B (2013) Role of surface charge on boundary slip in fluid flow. J Colloid Interf Sci 392:117–121

Pan Y, Bhushan B, Zhao X (2014) The study of surface wetting, nanobubbles and boundary slip with an applied voltage: a review. Beilstein J Nanotech 5:1042–1065

Seddon JRT, Lohse D (2011) Nanobubbles and micropancakes: gaseous domains on immersed substrates. J Phys Condens Matter 23:133001

Seddon JRT, Kooij ES, Poelsema B, Zandvliet HJW, Lohse D (2011) Surface bubble nucleation stability. Phys Rev Lett 106:056101

Shirtcliffe NJ, McHale G, Newton MI, Zhang Y (2009) Superhydrophobic copper tubes with possible flow enhancement and drag reduction. ACS Appl Mater Interf 1:1316–1323

Tretheway DC, Meinhart CD (2004) A generating mechanism for apparent fluid slip in hydrophobic microchannels. Phys Fluids 16:1509–1515

Uchida T, Oshita S, Ohmori M, Tsuno T, Soejima K, Shinozaki S, Take Y, Mitsuda K (2011) Transmission electron microscopic observations of nanobubbles and their capture of impurities in wastewater. Nanoscale Res Lett 6:295–304

Vinogradova OI (1995) Drainage of a thin liquid-film confined between hydrophobic surfaces. Langmuir 11:2213–2220

Wang Y, Bhushan B (2010) Boundary slip and nanobubble study in micro/nanofluidics with atomic force microscope. Soft Matter 6:29–66

Wang Y, Bhushan B, Maali A (2009a) Atomic force microscopy measurement of boundary slip on hydrophilic, hydrophobic, and superhydrophobic surfaces. J Vac Sci Technol A 27:754–760

Wang Y, Bhushan B, Zhao X (2009b) Nanoindents produced by nanobubbles on ultrathin polystyrene films in water. Nanotechnology 20:045301

Watanabe K, Udagawa Y, Udagawa H (1999) Drag reduction of Newtonian fluid in circular pipe with a highly water-repellent wall. J Fluid Mech 381:225–238

Yang JW, Duan JM, Fornasiero D, Ralston J (2003) Very small bubble formation at the solid–water interface. J Phys Chem B 107:6139–6147

Zhang XH, Zhang X, Sun J, Zhang Z, Li G, Fang H, Xiao X, Zeng X, Hu J (2007) Detection of novel gaseous states at the highly oriented pyrolytic graphite–water interface. Langmuir 23:1778–1783